DIPLOMARBEIT

Getting Ready for VLBI Observations to the Moon

zur Erlangung des akademischen Grades

Diplom-Ingenieurin

ausgeführt am Department für

Geodäsie und Geoinformation

Forschungsbereich Höhere Geodäsie

der Technischen Universität Wien

unter Anleitung von

Univ.Prof. Dipl.-Ing. Dr.techn. Johannes Böhm

und

Projektass.in(FWF) Dipl.-Ing.in Helene Wolf

durch

Olivia Franziska Panzenböck BSc

Matrikelnummer: 11775488

Wien, September 2024

Eidesstattliche Erklärung

Ich erkläre an Eides statt, dass die vorliegende Arbeit nach den anerkannten Grundsätzen für wissenschaftliche Abhandlungen von mir selbstständig erstellt wurde. Alle verwendeten Hilfsmittel, insbesondere die zugrunde gelegte Literatur, sind in dieser Arbeit genannt und aufgelistet. Die aus den Quellen wörtlich entnommenen Stellen sind als solche kenntlich gemacht.

Das Thema dieser Arbeit wurde von mir bisher weder im In- noch Ausland einer Beurteilerin/einem Beurteiler zur Begutachtung in irgendeiner Form als Prüfungsarbeit vorgelegt. Diese Arbeit stimmt mit der von den Begutachterinnen/Begutachtern beurteilten Arbeit überein.

Wien, September 2024

Lanzenböck Aura

Unterschrift Verfasserin

Acknowledgements

I sincerely thank Professor Johannes Böhm for his support and guidance over the years and for being a receptive and understanding listener to all my concerns.

Furthermore, I am very grateful to Helene Wolf, who provided outstanding mentorship and assistance in preparing my thesis. I would also like to acknowledge her and Lisa Kern for the great years we shared as office colleagues. In addition, I express my gratitude to my other colleagues in the Higher Geodesy research group for their fruitful collaboration. I am deeply grateful for the opportunity to have been part of the Higher Geodesy research group for several years.

I would also like to thank my fellow students for the numerous hours of intensive study, the good friendships that have developed and the wonderful time we have had.

Finally, I am deeply grateful to my family for their unwavering commitment and assistance. They make it possible for me to realise my dreams.

Licences

The following software, programs and data were used in the preparation of this thesis:

- Python 3.11 with the libraries Skyfield 1.48 (Rhodes, 2019), Cartopy 0.22.0 (Met Office, 2010), NumPy 1.26.4, Pandas 2.2.1, Matplotlib 3.8.3
- Matlab R2023b
- VieSched++ (Schartner and Böhm, 2019)
- TOPCAT 4.9 (Taylor, 2005)
- DeepL and Grammarly
- Lunar Laser Ranging (LLR) data from the Paris Observatory Lunar Analysis Centre (POLAC; Barache et al., 2021).
- Data from the Navigation and Ancillary Information Facility (NAIF; Acton et al., 2018; Acton, 1996).

Kurzfassung

Die geodätische Very Long Baseline Interferometry (VLBI) basiert auf der Beobachtung extragalaktischer Radioquellen, zumeist Quasaren. In den vergangenen Jahren wurde die Idee entwickelt, auch künstliche und natürliche Himmelskörper wie Satelliten und den Mond mit einem VLBI Transmitter auszustatten. Dieses Konzept eröffnet neue Perspektiven in den Bereichen Geodäsie, Astronomie und Raumfahrt. Die vorliegende Arbeit beschäftigt sich mit den dafür notwendigen Modellen der Auswertung, dargestellt mit der präzisen Positionierung eines VLBI Transmitters am Standort des Apollo 15 Reflektors auf dem Mond. Zur Evaluierung der ermittelten Position erfolgt eine Analyse von Lunar Laser Ranging (LLR) Messungen. Beim LLR wird die Laufzeit gemessen, die Laserlichtpulse von der LLR Station bis zum LLR Reflektor auf der Mondoberfläche und zurück brauchen. Aufgrund der großen Entfernung zwischen den beteiligten Objekten kommt es zu Verzögerungen der Laserpulse. Diese Verzögerungen müssen in der LLR Analyse entsprechend berücksichtigt werden. Im Rahmen dieser Arbeit erfolgt eine Fokussierung auf die beiden dominierenden Laufzeitverzögerungen, nämlich die atmosphärische Verzögerung und die Shapiro-Verzögerung. Infolge der Atmosphäre kommt es zu einer Lichtlaufzeitverzögerung von 2 bis 9 m. Die Shapiro-Verzögerung lässt sich in zwei Komponenten untergliedern. Die Sonne ist für Verzögerungen im Bereich von 6 bis 8 m verantwortlich, während die Erde Verzögerungen im Bereich von wenigen Zentimetern verursacht. Nach der Modellierung dieser Verzögerungen ergeben sich ab dem Jahr 2002 bis 2021 (keine Messungen vorhanden für 2006, 2007 und 2008) Residuen im Bereich von -1 bis +1 m. Im zweiten Teil dieser Arbeit erfolgt eine Sichtbarkeitsanalyse für den VLBI Transmitter auf der Mondoberfläche. Zu diesem Zweck erfolgt eine Modifikation der VLBI Scheduling-Software VieSched++. Die Evaluierung der Sichtbarkeit erfolgt anhand der Elevation sowie der Anzahl der Stationen, von denen aus der VLBI Transmitter gleichzeitig sichtbar ist. Es konnte festgestellt werden, dass die Anzahl der Stunden pro Tag, in denen der VLBI Transmitter sichtbar ist, in Abhängigkeit vom Standort der VLBI Station signifikanten Schwankungen unterliegt. Des Weiteren ist die Dauer der Sichtbarkeit des VLBI Transmitters von der Position des Mondes abhängig. Folglich ist die Erstellung eines adäquaten Beobachtungsplans sowie die Verwendung eines VLBI Netzwerkes mit global verteilten Stationen eine wesentliche Voraussetzung für erfolgreiche VLBI Beobachtungen zum Mond.

Abstract

Geodetic Very Long Baseline Interferometry (VLBI) is based on the observation of extragalactic radio sources, primarily quasars. In recent years, the concept of equipping artificial and natural celestial bodies, such as satellites and the Moon, with VLBI transmitters has emerged. This concept opens up new perspectives in the fields of geodesy, astronomy and spacecraft navigation. This thesis deals with the required models for the analysis, described by the precise positioning of a VLBI transmitter at the location of the Apollo 15 reflector on the Moon. The determined position is evaluated by analysing Lunar Laser Ranging (LLR) measurements. LLR measures the flight time of laser light pulses to travel from the LLR station to the LLR reflector on the lunar surface and back. Due to the considerable distance between the objects involved, the laser pulses are affected by several delays. These must be considered in the LLR analysis. In particular, this thesis focuses on the two dominant propagation delays, namely the atmospheric delay and the Shapiro time delay. The atmosphere causes a light propagation delay of 2 to 9 m. The Shapiro time delay can be subdivided into two components. The Sun is responsible for delays in the range of 6 to 8 m, while the Earth causes delays of a few centimetres. After modelling these delays, the residuals from 2002 to 2021 (no measurements available for 2006, 2007 and 2008) lie between -1 and +1 m. The second part of this thesis presents a visibility analysis of the VLBI transmitter on the lunar surface. For this purpose, modifications are made to the VLBI scheduling software VieSched++. The visibility is evaluated based on the elevation and the number of stations from which the VLBI transmitter is simultaneously visible. It was found that the number of hours per day during which the VLBI transmitter is visible varies considerably depending on the location of the VLBI station. Furthermore, the VLBI transmitter's visibility duration depends on the Moon's position. Therefore, to conduct successful VLBI observations to the Moon, it is essential to create an appropriate observation plan involving a globally distributed network of VLBI stations.

Contents

List of Figures

List of Tables

List of Abbreviations

arcsec Arcsecond

BCRS Barycentric Celestial Reference System

BIPM Bureau International des Poids et Mesures

CRF Celestial Reference Frame

DE Development Ephemeris

DOP Dilution of Precision

DORIS Doppler Orbitography and Radiopositioning Integrated by Satellite

EOP Earth Orientation Parameters

ESA European Space Agency

FWF Austrian Science Fund

GCRS Geocentric Celestial Reference System

GNSS Global Navigation Satellite System

GSFC Goddard Space Flight Center

ICRF International Celestial Reference Frame

ICRS International Celestial Reference System

IERS International Earth Rotation and Reference Systems Service

ILRS International Laser Ranging Service

ITRF International Terrestrial Reference Frame

ITRS International Terrestrial Reference System

IVS International VLBI Service for Geodesy and Astrometry

JD Julian Date

JPL Jet Propulsion Laboratory

LLR Lunar Laser Ranging

LSM Least Squares Method

mas Milliarcsecond

ME Mean Earth/Polar Axis (reference system of the Moon)

mJ Megajoule

MJD Modified Julian Date

ms Millisecond

NAIF Navigation and Ancillary Information Facility

NASA National Aeronautics and Space Administration

nm Nanometer

NP Normal Point

OCA Côte d'Azur Observatory, Grasse, France

PA Principal Axis (reference system of the Moon)

POLAC Paris Observatory Lunar Analysis Center

ps Picosecond

RMS Root Mean Square

SCRS Selenocentric Celestial Reference System

SLR Satellite Laser Ranging

SNR Signal-to-Noise Ratio

TAI International Atomic Time

TDB Barycentric Dynamical Time

TDT Terrestrial Dynamical Time

TRF Terrestrial Reference Frame

TRS Terrestrial Reference System

TT Terrestrial Time

UTC Coordinated Universal Time

UT Universal Time

VieVS Vienna VLBI and Satellite Software

VLBI Very Long Baseline Interferometry

1 Introduction

Space geodetic techniques, including Doppler Orbitography and Radiopositioning Integrated by Satellite (DORIS), Very Long Baseline Interferometry (VLBI), Global Navigation Satellite System (GNSS) and Satellite/Lunar Laser Ranging (SLR/LLR) are essential for positioning on Earth and in space. In VLBI, two or more radio telescopes on Earth simultaneously observe the incoming radio waves from extragalactic radio sources. The primary observable in VLBI is the time difference in arrival times for a pair of stations, which is determined based on the observed signals at the stations. VLBI plays a significant role in developing the International Terrestrial Reference Frame (ITRF) and the International Celestial Reference Frame (ICRF). Additionally, it is the sole space geodetic method capable of providing all Earth Orientation Parameters (EOP; Schuh and Böhm, 2013).

1.1 Motivation

The Moon is becoming an increasingly important object of scientific and technological study. In the future, it will assume a central role in several fields, including space travel, astronomy and geodesy. Space agencies, including the European Space Agency (ESA) and the National Aeronautics and Space Administration (NASA), have scheduled a series of prospective lunar missions.

NASA's Artemis mission aims to return humans to the Moon for the first time in over 50 years. This will facilitate a more comprehensive exploration of the Moon and the acquisition of knowledge regarding the capability for human habitation on the Moon. Furthermore, the mission is intended to serve as a preliminary step towards subsequent missions to Mars (Creech et al., 2022).

In recent years, the concept of equipping satellites and the Moon with VLBI transmitters to observe artificial sources has emerged. The VLBI transmitters emit pseudo-random noise signals across a broadband spectrum, similar to that observed in extragalactic radio sources. The ESA's GENESIS mission, which has already been approved, aims to combine up to four space geodetic techniques (VLBI, DORIS, SLR, GNSS) on a single satellite. This will contribute, among others, to an improved ITRF (Delva et al., 2022). Furthermore, there are plans to install VLBI transmitters on future generations of Galileo satellites.

In the context of the Moon, preliminary investigations have been conducted by Kłopotek et al. (2017), Kłopotek et al. (2019), Liu et al. (2020) and Zhao et al. (2022), which have explored the potential benefits of installing a VLBI transmitter on the Moon. For this purpose, data from simulations and Chinese missions are used. Installing a VLBI transmitter should contribute to the establishment of a stable lunar geodetic reference frame and provide new insights into the Moon.

1.2 Study Objectives

This thesis explores the models required to analyse VLBI observations to the Moon. The process is examined through the analysis of LLR measurements. On the one hand, the aim is to establish the foundations for the scheduling and simulation of VLBI observations to the Moon in the VLBI scheduling software VieSched++, as well as for the subsequent analysis of these observations in the Vienna VLBI and Satellite Software (VieVS). On the other hand, analysing LLR measurements should facilitate a more profound comprehension of lunar coordinate systems and lay the groundwork for analysing LLR measurements with VieVS in the future. The combination of VLBI and LLR also opens up new possibilities. By placing a reflector close to the VLBI transmitter, with the distance between the two components being precisely known. LLR measurements can then determine the distance from the Earth to the measurement point on the Moon, while the direction is derived from VLBI observations. The aim of the LLR analysis in this thesis is to model the two most significant delays to achieve residuals with an accuracy of $\pm 1\ m$ for measurements from the Côte d'Azur Observatory (OCA) in Grasse, France, to the Apollo 15 reflector. In the second part of the thesis, the positioning of the VLBI transmitter is implemented in the scheduling software VieSched++, and a visibility analysis for the VLBI transmitter on the Moon is conducted. This process involves checking when an observation between selected VLBI stations and the VLBI transmitter is possible by examining the elevation and the number of VLBI stations with a simultaneous line of sight to the VLBI transmitter.

1.3 Arrangement of the Thesis

Chapter 2 provides an overview of the relevant theoretical framework for the thesis. The chapter explains the principles of VLBI and LLR and gives an overview of the various reference frames and time scales. Chapter 3 describes the analysis of the LLR measurements. The analysis includes the transformation between the reference frames and the time scales, as well as the modelling of the delays. In Chapter 4, a visibility analysis for the VLBI transmitter for a selected VLBI network is conducted. Chapter 5 summarises the thesis and provides an outlook on potential future investigations.

2 Theoretical Framework

This chapter summarises the most crucial theoretical information relevant to this thesis. The first two subsections offer insight into two geodetic space techniques: Very Long Baseline Interferometry (VLBI) and Lunar Laser Ranging (LLR). The last two sections provide an overview of the various reference frames and time scales.

2.1 Very Long Baseline Interferometry

The foundation for VLBI was established following the discovery by American physicist and radio engineer Karl Guthe Jansky in 1931/1932 that celestial bodies emit radio beams (Kellermann et al., 2020).
Today, extragalactic radio sources that emit particularly intense radio beams are observed using VLBI. Radio telescopes distributed around the globe are used to receive and process these radio beams. The International VLBI Service for Geodesy and Astrometry (IVS) is responsible for coordinating the observations and providing the products. VLBI is a fundamental component for the establishment of the ICRF and, in conjunction with further geodetic space techniques, plays a significant role in developing the ITRF. Moreover, VLBI is the sole geodetic space technique capable of determining all EOP. In particular, VLBI is the only method to determine the Universal Time (UT1) accurately (Schuh and Behrend, 2012).

2.1.1 Measurement Principle

In VLBI, two or more VLBI radio telescopes on Earth simultaneously observe an extragalactic radio source. The observed sources are billions of light years away from Earth. Consequently, the radio waves emitted by these sources arrive at the receiving stations as plane wavefronts. Figure 2.1 illustrates this principle. The vector k indicates the direction of the observed source and is parallel for all VLBI stations on Earth due to the large distance of the radio source. The VLBI stations 1 and 2 are connected by the baseline vector b.

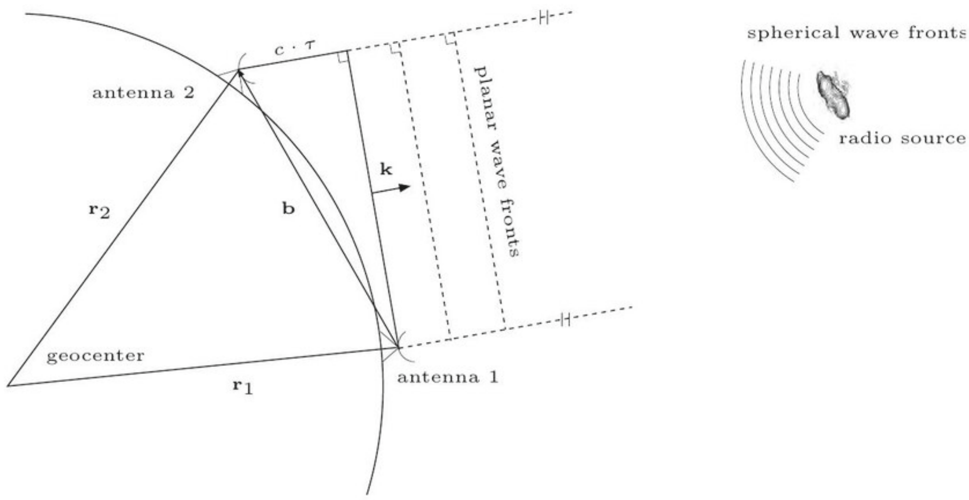

Figure 2.1: The basic principle of VLBI, from Artz (2011).

Each incoming signal is time-stamped, digitised and recorded at the radio telescopes. Subsequently, the data is transferred to the correlators, which correlate and fringe-fit the data. One product is the time difference τ, called group delay. This time difference arises because the wavefront arrives at the stations at different times. τ is calculated using Equation 2.1 and is the negative scalar product of the baseline vector between the two VLBI stations and the direction to the radio source, scaled by the speed of light c (Schuh and Böhm, 2013).

$$\tau = -\frac{b \cdot k}{c} = t_2 - t_1 \tag{2.1}$$

2.1.2 Scheduling

As it is required that at least two stations observe the same source, a schedule must be created before VLBI measurements can be done. This schedule provides precise regulation regarding the observation of sources by each station. This process is very complex, as many different parameters must be considered. A good schedule is essential, as an efficient and well-thought-out approach to the observations leads to better results, and geodetic parameters of higher quality can be determined (Schartner and Böhm, 2019). There are very few VLBI scheduling software worldwide. In this thesis, the scheduling software VieSched++ by Schartner and Böhm (2019) is used for the purpose of conducting the visibility study presented in Chapter 4.

A geodetic session typically lasts 1 or 24 hours. A schedule is created for this duration, consisting of a sequence of scans. A scan refers to the period when several telescopes observe the same source. The scheduling software creates a schedule scan by scan. For each scan, all possible combinations of stations and sources are determined. Finally, these combinations are compared using metrics such as scan duration, number of observations and sky coverage. The most advantageous scan is selected, and the procedure starts again until the schedule is complete. The challenge is that it is not possible to fulfil all criteria optimally, and a compromise must be found to achieve the best result. Moreover, it is essential to acknowledge the heterogeneous characteristics of the distributed stations. These include, among others, differences in slew speeds, sensitivities, visibility areas, and antenna mounts (Schartner and Böhm, 2019).

2.1.3 Analysis

The final step is the analysis of the VLBI data. Figure 2.2 illustrates the main steps as a flowchart. On the left-hand side of the flowchart, effects that influence the VLBI measurements and must be taken into account in the analysis can be seen. These include influences that the signal experiences on its long journey to Earth through the atmosphere and inaccuracies that originate from radio telescopes or radio sources. Models for this are provided by the International Earth Rotation and Reference Systems Service (IERS). The parameters for calculating the theoretical delay are shown in the right-hand column of the flowchart. These include the a priori station coordinates, the a priori source coordinates and a variety of models. The reduced observed delay and the theoretical delay are then combined to form the observed-computed (o-c) vector. The next step is the estimation of parameters using the Gauss-Markov least squares method (LSM). A single session is sufficient to estimate several parameters. For example, all five EOP can be determined using VLBI as the sole method. If several sessions are combined, a global solution can be calculated. This allows the estimation of a Terrestrial Reference Frame (TRF) or a Celestial Reference Frame (CRF) with high accuracy (Schuh and Böhm, 2013).

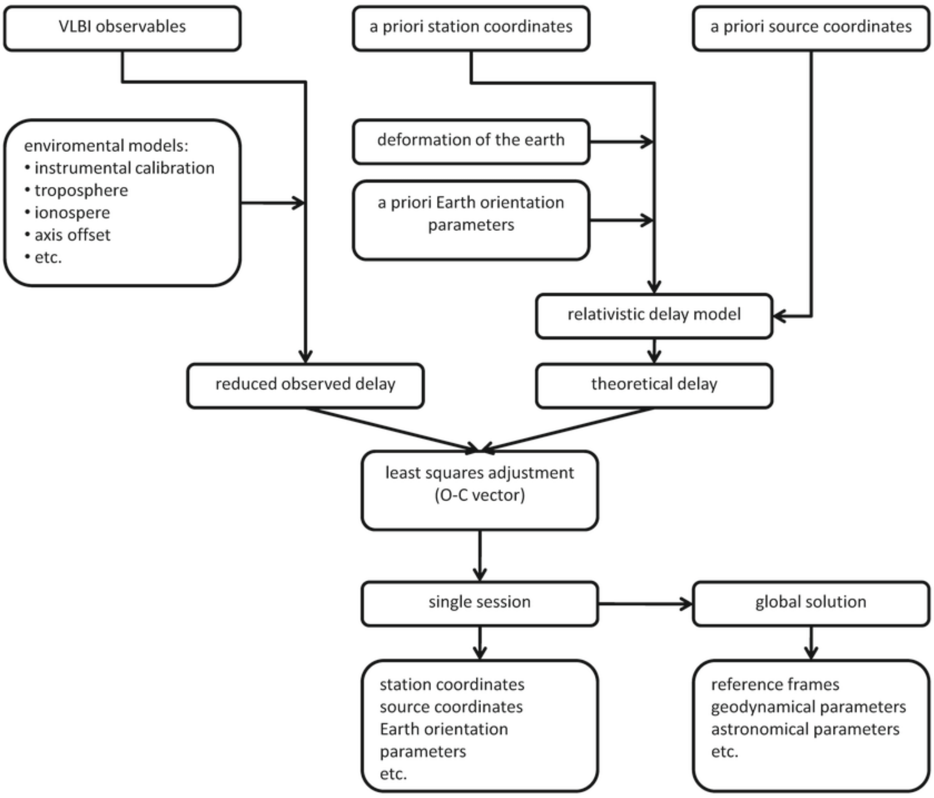

Figure 2.2: VLBI analysis flowchart, from Munghemezulu et al. (2014) based on Schuh and Böhm (2013).

2.1.4 VLBI Targets in Future Observations

The VLBI technique is based on the observation of extragalactic radio sources. In recent years, the concept of equipping celestial bodies with a VLBI transmitter to obtain a greater diversity of observations has emerged. Those celestial bodies suitable for this purpose include satellites and the Moon.

The ESA plans to equip some of the GNSS Galileo satellites with VLBI transmitters. A number of studies have already examined the advantages of observing satellites with VLBI. The VLBI2Galileo project is an Austrian Science Fund (FWF) project conducted in collaboration with the Eidgenössische Technische Hochschule Zürich (ETH Zürich) and the Technische Universität München (TU München). The VLBI2Galileo project is concerned with scheduling, simulation, and analysis of combined satellite and quasar observations. For this purpose, the software VieSched++ was extended with a satellite module (Wolf, 2021). The following papers have been published so far in the VLBI2Galileo project: Wolf et al. (2023), Wolf and Böhm (2023), Böhm and Wolf (2024).

2.2 Lunar Laser Ranging

Since 1969, the distance between the Earth and the Moon has been measured with high precision using LLR. The extensive time series of LLR observations thus enables the determination of numerous parameters. These include the identification of station coordinates and reflector coordinates, the calculation of relativistic parameters, the establishment of ephemerides, the definition of EOP, the delineation of parameters of the Earth-Moon system, and the characterisation of parameters describing the physics of the Moon (Müller et al., 2019).

2.2.1 Measurement Principle

In LLR, short laser light pulses are transmitted from a LLR station on Earth to the surface of the Moon. Upon reaching the Moon, the laser light pulses are reflected by the targeted LLR reflector and return to the station. The time the laser light pulse departs from the station and the time it reaches the station on Earth are recorded with high accuracy. At the beginning of LLR measurements, the distance measurement accuracy was approximately a few decimetres. The present level of accuracy is in the range of a few millimetres (Müller et al., 2019; Murphy, 2013b). The fundamental principle of LLR is illustrated in Figure 2.3.

LLR observations are conducted at intervals of between 5 and 15 minutes. The telescope generates laser pulses with a pulse duration of 70 to 200 ps, an energy of 100 to 200 mJ, and repetition rates of 10 to 20 Hz. A laser light pulse with a wavelength of 532 nm and a pulse energy of 100 mJ contains approximately $3 \cdot 10^{17}$ photons. After leaving the telescope, the laser light pulse takes the form of a disc. The diameter of this disc depends on the telescope, with a thickness of a few centimetres. On the way to the Moon, atmospheric turbulences cause divergences in the order of arcseconds. The laser light pulse illuminates an area of several km^2 on the Moon. As a reference, a beam of 1 arcsec illuminates the Moon over a distance of 1.9 km. For the Apollo 11 reflector, the probability of a photon hitting the reflector is 1 in 25 million. When the light is reflected, diffraction phenomena cause it to diverge again in the arcsecond range. The returning laser beam illuminates a circular area on the Earth's surface with a diameter of about 15 km. Consequently, only a subset of the photons are returned to the telescope aperture. All the signal losses (caused by the atmosphere, the transmitting and receiving units and others) result in a total loss in the order of 10^{18}. The measurements taken at 5 to 15 minute intervals are summarized to a Normal Point (NP) and then written to a file along with atmospheric parameters and other key figures (Müller et al., 2019; Murphy, 2013b; Murphy et al., 2008).

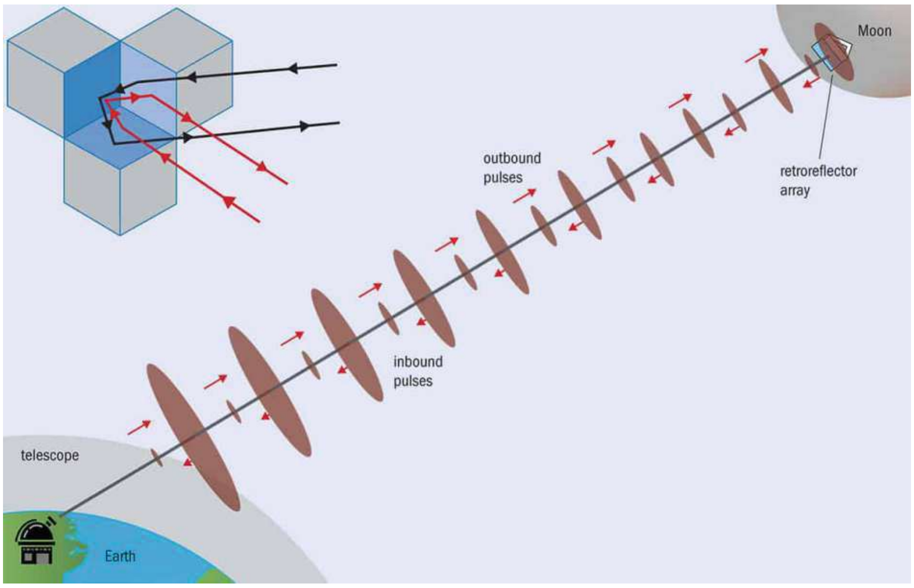

Figure 2.3: The basic principle of LLR, from Crease (2019).

2.2.2 Retroreflectors on the Moon

As of 2023, five retroreflectors have been deployed on the surface of the Moon. The locations of the five reflectors on the lunar surface are illustrated in Figure 2.4. As the name indicates, the defining characteristic of these reflectors is that they emit light in a direction parallel to that from which it was emitted. The fundamental concept is demonstrated in Figure 2.3, located in the upper left corner.

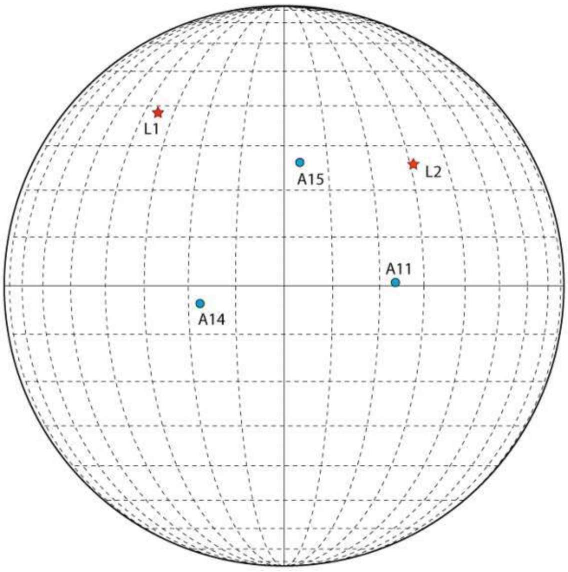

Figure 2.4: Positions of the five retroreflectors on the lunar surface with „A“ denoting Apollo and „L“ designates Lunokhod, from Murphy (2013a).

Three reflectors were installed on the Moon during the Apollo 11 (1969), Apollo 14 (1971) and Apollo 15 (1971) missions, and were named after those missions. Two additional identical reflectors are located on the Lunokhod 1 and Lunokhod 2 rovers, which were brought to the Moon as part of the Luna 17 (1970) and Luna 21 (1973) Soviet missions. The Apollo 11 and Apollo 14 reflectors comprise 100 corner cube reflectors, whereas the Apollo 15 reflector consists of 300, each with a diameter of 3.8 cm. The reflector arrays on the Lunokhod rover include 14 triangular-faced corner cubes, each with an edge length of 11 cm. The power of the Lunokhod arrays is intermediate between that of the 100-element Apollo array and the 300-element Apollo array (Müller et al., 2019).

2.2.3 LLR Stations on Earth

The underlying measurement principle is analogous to that employed in SLR, in which short laser light pulses are transmitted in the direction of the satellite, reflected there, and subsequently returned. It is important to note that the signal loss due to the distance is more significant in LLR measurements than in SLR measurements. The signal received from the Moon is 10^7 times weaker than the signal returned from a LAGEOS satellite. Consequently, only a limited number of laser ranging stations worldwide are technically capable of making measurements to the Moon (Müller et al., 2019). Laser ranging stations that are able to perform LLR measurements and which are included in the data set collected by the Paris Observatory Lunar Analysis Centre (POLAC) can be seen in Figure 2.5.

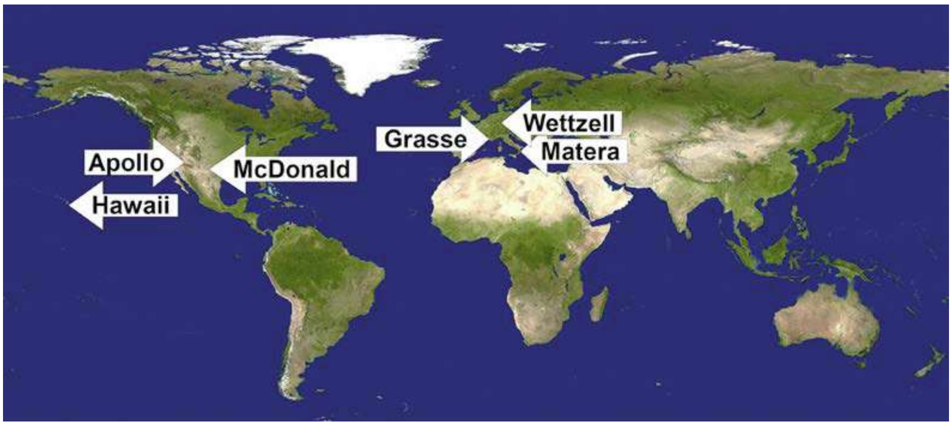

Figure 2.5: Positions of the LLR stations whose data is collected by POLAC, from Hofmann et al. (2015)

2.2.4 Measurement Conditions

In order to ensure the accuracy and success of LLR observations, it is essential to consider a number of key factors. In addition to meteorological conditions being suitable, the phase of the Moon is of great importance. It has been the standard practice for LLR stations to utilise a green laser beam with a wavelength of 532 nm. However, this precludes observation of the New Moon, as the sun's light causes excessive interference. Similarly, it is almost impossible to conduct measurements during a Full Moon, as the scattered light from the Moon results in significant interference (Biskupek, 2015).

Since 2015, the Grasse LLR station can also perform infrared measurements at a wavelength of 1064 nm. As demonstrated in Courde, C. et al. (2017), the utilisation of infrared technology has been shown to enhance the station's efficiency by a factor of eight during New Moon and Full Moon phases, thereby improving the consistency of LLR observations over a synodic month. A synodic month is the period it takes the Moon to complete an entire cycle of phases and return to the same relative position with respect to the Sun. The mean duration of a synodic month is approximately 29.53 days.

2.2.5 Normal Point Statistics

The number of measurements made by LLR stations varies depending on the specific station. In addition, the target frequency of the five LLR reflectors is variable. Figure 2.6 illustrates the percentage of measurements for each station and reflector from 1969 to 2021. The presented statistics are in alignment with the POLAC data. A total of 31 248 normal points were measured over the specified period. The Grasse station was responsible for the most significant number of LLR measurements, with a total of 58%, followed by the McDonald 2.7m, APOLLO and MLRS2 stations, which accounted for 12% of the total. In the past, the Apollo 15 reflector was, with 64%, the most frequently used target for lunar measurements, according to Hofmann et al. (2015) because of its size and the strongest associated signal strength. 12% of the measurements were made on the Apollo 14 and Apollo 11 reflectors.

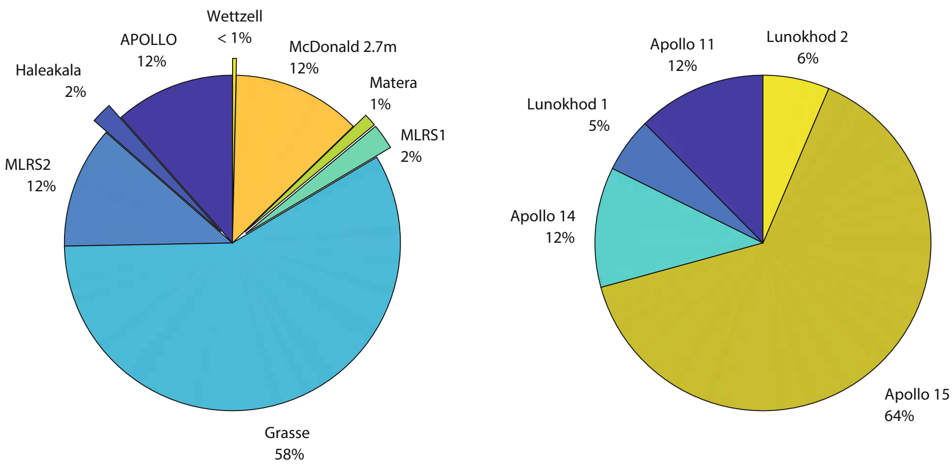

Figure 2.6: Normal point statistics for LLR stations (left) and LLR reflectors (right) from 1969 to 2021 based on data from the POLAC.

2.3 Reference Frames

Reference frames are of significant importance within the field of geodesy. They establish a uniform basis for geodetic measurements and are fundamental for precise positioning. A reference system defines a coordinate system through models, parameters, and constants, whereas a reference frame represents the realisation of such a system through, for instance, coordinates. A distinction is made between body-fixed reference systems and space-fixed reference systems.

2.3.1 Body-fixed Reference Systems

A body-fixed reference system is firmly connected to a body, such as the Earth or the Moon, and rotates with the respective body. The system's origin is located at the centre of mass of the body. The following section will discuss the body-fixed reference systems of the Earth and the Moon.

Earth

In order to determine positions on Earth, it is necessary to have a precisely defined coordinate system. The International Terrestrial Reference System (ITRS) is the Terrestrial Reference System (TRS) that is employed globally. The coordinates and velocities of stations are calculated from the data collected by geodetic space techniques, including VLBI, GNSS, DORIS and SLR/LLR. Subsequently, these are combined by the IERS and used to realise the ITRS. The result of this process is the ITRF. The current version of the ITRF is the ITRF2020, which is the successor of the ITRF2014 (Hellmers et al., 2023).

Moon

Two distinct reference frames have been established for the Moon. The two systems differ in their respective definitions of the orientation of their axes.

The first system is the Principal Axis (PA) reference system. The principal axes of inertia orient the axes of this system. The Z-axis of the PA system is aligned along the maximum axis of inertia of the Moon, which corresponds to the rotational axis of the Moon. The X-axis is aligned along the minimum axis of inertia, while the Y-axis is orthogonal to the other two axes. The origin of the PA system is located at the centre of mass of the Moon. The PA system is mainly used to model the Moon's gravitational field. The second system, the Mean Earth/Polar Axis (ME) reference system, differs from the previous one in that the X-axis points in the direction of the mean position of the Earth, while the Z-axis is aligned along the rotational axis of the Moon and the Y-axis completes the right-handed coordinate system. As with the PA system, the origin of the ME system is located at the centre of mass of the Moon. The ME system is used for applications in cartography and navigation (Biskupek, 2015).

The difference between a location in the ME and PA frames can be up to 875 metres, affecting both longitude and latitude. This value varies depending on the location on the Moon (Archinal et al., 2024).

2.3.2 Space-fixed Reference Systems

Space-fixed reference systems can be defined in two ways: kinematically or dynamically. Kinematically means that the system is defined by distant objects such as stars or extragalactic radio sources. In contrast, a dynamic system is defined by the equations of motion of the Sun, Moon and planets. The origin of space-fixed reference systems can be not only in celestial bodies but also in the barycentre of the solar system (Soffel and Langhans, 2013).

Examples of well-known systems are:

- Barycentric Celestial Reference System (BCRS): Origin in the solar system barycentre
- International Celestial Reference System (ICRS): Origin in the solar system barycentre
- Geocentric Celestial Reference System (GCRS): Origin in the geocentre
- Selenocentric Celestial Reference System (SCRS): Origin in the centre of mass of any celestial body (for example, the Moon)

The BCRS is a fundamental tool for analysing LLR data, as all calculations are performed within this system. The BCRS is an inertial system employed for various applications, including the determination of the position of celestial bodies, the navigation of spacecrafts, and the calculation of ephemerides (Soffel et al., 2003). As stated in IAU 2006 Resolution B2, the BCRS is aligned with the axes of the ICRS (unless otherwise indicated).

2.4 Time Scales

In addition to various reference systems, there are also various time scales. The essential time scales for this thesis are briefly explained below.

2.4.1 Julian Date (JD)

The Julian Date (JD) indicates how many days have passed since 1 January 4713 BC at 12:00 UT. A derived variant is the Modified Julian Date (MJD), which originated on 17 November 1858 at 00:00 UT. The connection to the JD is:

$$MJD = JD - 2\,400\,000.5 \tag{2.2}$$

It has become common practice to define a standard epoch for geodetic and astronomical calculations. The current epoch is J2000 and refers to 1 January 2000, 12 TT with JD = 2 451 545.0 and MJD = 51 544.0 (McCarthy, 1998). TT stands for Terrestrial Time and is explained in Section 2.4.5. Julian date is used in LLR analysis to transform between different time scales.

2.4.2 Universal Time (UT)

The Universal Time (UT) is split into UT0, UT1 and UT2. The three timeframes differ by a few milliseconds. The mean local time at Greenwich, derived directly from observations, is designated as UT0. Furthermore, UT1 is corrected for the effect of polar motion, while UT2 is additionally reduced by the effect of seasonal fluctuations in the Earth's rotation (Nelson et al., 2003).

2.4.3 Coordinated Universal Time (UTC)

The Coordinated Universal Time (UTC) has been the internationally recognised time standard since 1 January 1972 and is the basis for time zones worldwide. UTC combines Atomic Time (TAI) with Universal Time (UT1). UTC is determined by high-precision atomic clocks and is regularly adjusted by leap seconds to Universal Time UT1, which is based on the Earth's rotation. If

$$|UTC - UT1| \geq 0.9\,s \tag{2.3}$$

applies, a leap second is introduced in UTC. The IERS is responsible for the coordination of leap seconds. The unit of UTC is the SI second (Nelson et al., 2003).

2.4.4 International Atomic Time (TAI)

The International Atomic Time (TAI) is a time scale obtained by averaging many atomic clocks distributed worldwide. It is maintained by the Bureau International des Poids et Mesures (BIPM). TAI is defined in a geocentric reference frame and is based on the SI second (Petit et al., 2015). The link between UTC and TAI is given by (as of 2024):

$$TAI = UTC + 37\,s \tag{2.4}$$

2.4.5 Terrestrial Time (TT) and Barycentric Dynamical Time (TDB)

The Terrestrial Time (TT), formerly Terrestrial Dynamic Time (TDT), is derived from TAI and is defined on the rotating geoid. TT replaces the Ephemeris Time (ET) and is a uniform time scale. The unit of TT is the SI second. The relationship between TT and TAI is given by (defined on 1 January 1977, 00:00:00 TAI):

$$TT = TAI + 32.184\,s \tag{2.5}$$

In contrast, the Barycentric Dynamical Time (TDB) refers to the barycentre of the solar system. Since TDB takes time dilation into account, it plays an essential role in ephemeris calculations (Nelson et al., 2003). For LLR analyses, all time points must be converted to TDB.

2.5 The Earth-Moon System

The Earth-Moon system is a highly complex and dynamic mechanism. As shown in Figure 2.7, the Earth's axis of rotation is not normal to the ecliptic plane but is inclined by about 23.4°. The same applies to the Moon, whose axis of rotation is inclined by about 1.54° and whose orbit makes an angle of about 5.14° with the ecliptic plane.

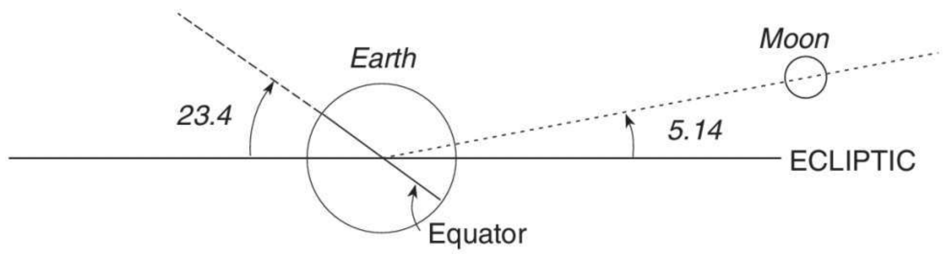

Figure 2.7: Constellation of the Earth and Moon in relation to each other, from Condie (2011).

The Moon orbits the Earth once every 27.32 days in relation to the stars, called a sidereal month. In relation to the Sun's position, the time it takes for the Moon to go through all its phases takes 29.53 days, known as a synodic or lunar month. The difference between the sidereal month and the synodic month (about 2.21 days) is because while the Moon orbits the Earth, the Earth continues to move around the Sun (Saleh, 2018).

The Earth and the Moon themselves rotate together around the Earth-Moon barycentre, which is the centre of mass of the Earth and the Moon. The Earth-Moon barycentre is still inside the Earth at a distance of about 4670 km from the centre of the Earth (McCall, 2005).

Another important aspect is that we always see the same side of the Moon. It means that the speed at which the Moon rotates around the Earth is the same as the speed at which the Moon rotates around its axis. Because the Moon is subject to the effect of optical libration, about 60% of the Moon's surface is visible from the Earth (Eppler and Budden, 2018).

The Moon moves around the Earth in an elliptical orbit. As a consequence, the distance between the Earth and the Moon changes constantly. The distance is defined as the distance between the Earth's centre and the Moon's centre. The largest distance in 2022 was 406 700 km, the smallest distance about 356 500 km (Gorkavyi et al., 2023).

3 Spatial examination of the distance Earth-Moon

With LLR, the distance between the Earth and the Moon can be determined with high precision. This chapter focuses on the LLR measurement analysis between the LLR station at the Côte d'Azur Observatory (OCA) in Grasse, France and the Apollo 15 reflector. A significant aspect of the analysis is the transformation between the Earth and Moon reference frames, transformations between the time scales and the modelling of signal delays. Two delays that lead to inaccuracies in the metre range are the atmospheric delay and the Shapiro time delay. Correcting these delays results in residuals ranging from approximately -1 to 1 m. In order to achieve a better accuracy, it would be necessary to consider further effects, as indicated in Chapter 3.2. However, these are not discussed further in this thesis, because an accuracy of $\pm 1\ m$ is sufficient for this study.

3.1 Methodology

3.1.1 Data and Tools

The analysis is conducted using the Python package Skyfield (Rhodes, 2019), which has been adapted for this purpose. The Earth-Moon system is a highly complex entity; therefore, several data sets are required for the analysis to achieve an accurate result. This thesis employs the highly precise DE440 ephemeris (Park et al., 2021), published by the Jet Propulsion Laboratory (JPL) in 2021. Moreover, SPICE kernels from NASA's Navigation and Ancillary Information Facility (NAIF) are used. The kernels contain data on the positions of celestial bodies, physical constants, information on coordinate systems, and other relevant data (Acton et al., 2018; Acton, 1996).

The following files are part of the modelling process:

- *de440.bsp*
  Published by JPL, the planetary and lunar ephemerides Development Ephemeris (DE) series includes the positions and corresponding velocities of the Sun and Moon, the barycentres of the eight planetary systems, the barycentre of the Pluto system, and the lunar libration angles (Park et al., 2021).

- *moon_de440_220930.tf*
  This kernel contains specifications for the PA and ME reference systems of the Moon (Park et al., 2021).

- *pck00011.tpc*
  This file contains orientation information for natural satellites, Sun, planets and selected asteroids (Archinal et al., 2018).

- *moon_pa_de440_200625.bpc*
  This file is used to orient the principal axis of the Moon (Park et al., 2021).

Transformations between terrestrial and celestial reference systems require the use of EOP. For this purpose, the standard rapid EOP data with a 24-hour resolution, provided by IERS since 1 January 1992 (IAU2000), are utilised. The LLR measurements used come from the POLAC (Barache et al., 2021). The POLAC team collects LLR data from the various stations and prepares them for further processing. This process entails the exclusion of measurements that are grossly erroneous or duplicative. The published files contain the start time of the measurement. The measurement itself is expressed as the transit time from Earth to the Moon and back in seconds. Additionally, the files comprise supplementary data, including atmospheric parameters, such as pressure, temperature and humidity. Furthermore, the uncertainty of the measurement, the Signal-to-Noise Ratio (SNR), the number of photons and other parameters are also provided.

3.1.2 Position of the VLBI Transmitter on the Moon

So far, no official position of a possible VLBI transmitter has been published. However, there are already studies, such as the one by Sert (2023), dealing with the optimal position of a VLBI transmitter on the lunar surface. It can be concluded that the correct position of the VLBI transmitter is of significant importance. For the sake of simplicity, this thesis assumes the position of the Apollo 15 reflector as the position of a VLBI transmitter. The reflector's position on the lunar surface can be seen in Figure 2.4. The DE440 coordinates of the Apollo 15 reflector in the PA frame are used for the calculations, which are given in Table 3.1.

Table 3.1: Coordinates of the Apollo 15 reflector in the DE440 PA frame from Park et al. (2021).

	x [m]	y [m]	z [m]
Apollo 15 reflector	1 554 678.104	98 094.498	765 005.863

3.1.3 LLR Station on Earth

Measurements from the LLR station at the Côte d'Azur Observatory (OCA) in Grasse, France, to the Apollo 15 reflector are used to model the distance between the Earth and the Moon. The Grasse LLR station was chosen because it has recorded the most LLR measurements in the history of measurements. The same applies to the Apollo 15 reflector, which has the most measurements since the beginning. The coordinates of the Grasse LLR station are given in the ITRF2020 and are provided in Table 3.2.

Table 3.2: Coordinates of the OCA LLR station in Grasse, France, given in the ITRF2020 (Altamimi et al., 2022).

	DOMES	Code	x [m]	y [m]	z [m]
OCA	10002S002	7845	4 581 691.9389	556 196.3678	4 389 355.2869

3.2 Analysis of LLR Data

The LLR data is analysed according to the principle described in Biskupek (2015). LLR is a method based on time-of-flight measurements. The distance can be calculated from the time it takes light to travel from the Earth to the Moon and back. Therefore, the light travel time is multiplied by the speed of light denoted as c, and divided by two to give the one-way distance. This yields the approximate Equation 3.1 for the measured distance:

$$\rho_m = \frac{\tau}{2} c \tag{3.1}$$

An exact mathematical determination of the distance can be made using Equation 3.2. Since the up-leg and down-leg paths of the laser pulse are not identical, the time of reflection t_2 at the Moon and the time of reception t_3 at the LLR station must be determined in addition to the given start time t_1. This allows the light propagation time for the up-leg τ_{12} and the down-leg τ_{23} paths to be determined separately. Some corrections must be made since the signal experiences delays on the way to the

Moon and back. τ_{rel} is the delay that the light experiences in gravitational fields of massive bodies, caused by the space-time curvature according to the general theory of relativity. This phenomenon is referred to as the Shapiro time delay (Shapiro, 1964). τ_{atmo} contains the effects that the light experiences due to the atmosphere (Mendes and Pavlis, 2004; Mendes et al., 2002).

$$\rho_c = \frac{\tau_{12} + \tau_{23} + \Delta\tau_{rel} + \Delta\tau_{atmo} + \Delta\tau_{syn} + \Delta\tau_{syst}}{2} c \tag{3.2}$$

$\Delta\tau_{rel}$ and $\Delta\tau_{atmo}$ are corrections in the metre range and are explained in more detail in the sections 3.2.3 and 3.2.4. This yields residuals $(\rho_m - \rho_c)$ within the range of $\pm 1\ m$. In order to achieve greater accuracy, it is necessary to consider additional effects. As stated in Biskupek (2015), thermal effects and the synodic oscillation of the Moon's orbit due to the radiation pressure of the sun $\Delta\tau_{syn}$ (details in Vokrouhlický (1997)) must be taken into account. Furthermore, corrections must be considered due to systematic errors at the LLR stations, designated as $\Delta\tau_{syst}$. It should be noted, that this thesis does not address these effects. Therefore, they have been added in Equation 3.2 in a grey colour. All calculations are performed in the BCRS, thus requiring all necessary positions to be transformed into this system. Consequently, all time points must be transformed from UTC to TDB.

The reflection time t_2 and the reception time t_3 are determined through an iterative process. The flight time is calculated on the basis of the initial distance between the two bodies. In each iteration, the position of the Moon and the Earth is corrected, and the time of flight is recalculated. The necessity for iteration arises from the fact that the light traverses the distance between the Earth and the Moon in approximately 1.3 seconds, a period during which the Earth and Moon continue to move. The iteration is concluded when the discrepancy between successive estimates of the light travel time is less than 10^{-12} or when the maximum number of iterations (10) is reached. The iteration is conducted separately for the up-leg and down-leg paths. The times t_1, t_2 and t_3 can be employed to calculate the flight times τ_{12} and τ_{23}, using Equation 3.3. Figure 3.1 illustrates the measurement configuration and the vectors required for the calculations.

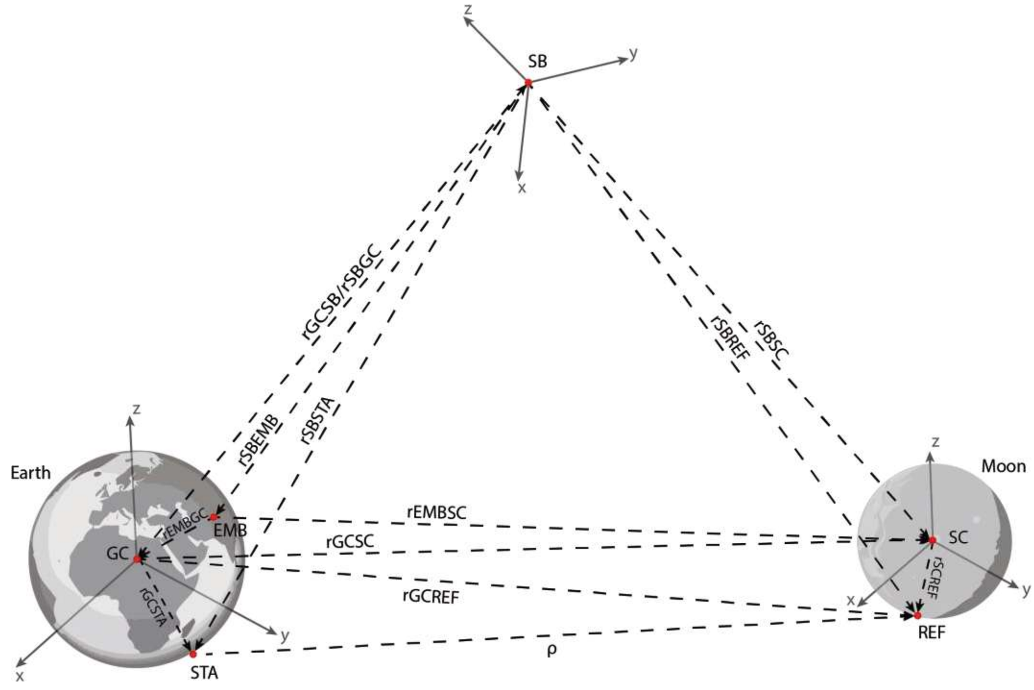

Figure 3.1: Sketch of the LLR analysis configuration. It depicts the Earth and Moon with their respective centres of mass, the LLR station, the retroreflector on the Moon, the solar system barycentre and the Earth-Moon barycentre. All vectors are defined in the BCRS. This figure is based on the illustration in Biskupek (2015).

The abbreviations used in the Equations 3.3, 3.4, 3.9, 3.10, 3.11, 3.12 and Figure 3.1 are explained below. All vectors are defined in the BCRS.

- SB - Solar system barycentre
- GC - Geocentre
- SC - Selenocentre
- EMB - Earth-Moon barycentre
- STA - LLR Station (on the Earth)
- REF - LLR Reflector (on the Moon)
- r_{SBEMB} - Vector from the solar system barycentre to the Earth-Moon barycentre
- r_{SBGC} - Vector from the solar system barycentre to the geocentre

- r_{SBREF} - Vector from the solar system barycentre to the reflector
- r_{SBSC} - Vector from the solar system barycentre to the selenocentre
- r_{SBSTA} - Vector from the solar system barycentre to the station
- r_{EMBGC} - Vector from the Earth-Moon barycentre to the geocentre
- r_{EMBSC} - Vector from the Earth-Moon barycentre to the selenocentre
- r_{GCSB} - Vector from the geocentre to the solar system barycentre
- r_{GCREF} - Vector from the geocentre to the reflector
- r_{GCSC} - Vector from the geocentre to the selenocentre
- r_{GCSTA} - Vector from the geocentre to the station
- r_{SCREF} - Vector from the selenocentre to the reflector
- ρ - Distance between the station and the reflector

The runtime for the up-leg τ_{12} and down-leg τ_{23} path is calculated using the equation 3.3:

$$\begin{aligned}\tau_{12} &= \frac{r_{SBREF}(t_2) - r_{SBSTA}(t_1)}{c}\\ \tau_{23} &= \frac{r_{SBREF}(t_2) - r_{SBSTA}(t_3)}{c}\end{aligned} \tag{3.3}$$

The respective vectors are derived from Equation 3.4:

$$\begin{aligned}r_{SBSTA}(t_1) &= r_{GCSTA}(t_1) - r_{GCSB}(t_1)\\ r_{SBREF}(t_2) &= r_{SCREF}(t_2) + r_{GCSC}(t_2) - r_{GCSB}(t_2)\\ r_{SBSTA}(t_3) &= r_{GCSTA}(t_3) - r_{GCSB}(t_3)\end{aligned} \tag{3.4}$$

3.2.1 Coordinate Transformation

In order to calculate the distance between the Earth and the Moon, it is necessary to have the positions of both celestial bodies, as well as the coordinates of the station and the reflector, in the BCRS. The coordinates of the retroreflector are initially provided in the moon-fixed PA frame (see Table 3.1), while the station coordinates are given in the ITRF2020 (see Table 3.2). The requisite transformations are then performed in the Python package Skyfield, utilising the Chebyshev approximation outlined in Liu et al. (1980). Chebyshev polynomials are orthogonal over the interval

$[-1,1]$ with respect to the weight function $\omega(x) = \frac{1}{\sqrt{1-x^2}}$. Chebyshev polynomials are optimal in minimising the maximum error in an approximation, making them particularly efficient. In practice, this implies that they are more resistant to numerical errors. The function is approximated over the interval $[a,b]$. For the Chebyshev approximation, it is necessary to scale the interval to $[-1,1]$. The normalised time variable is given by Equation 3.5 with f_a and f_b representing the start and end times, respectively.

$$\tau = 2\frac{t - t_a}{t_b - t_a} - 1 \tag{3.5}$$

The following solutions result for the polynomials of degree 0 and degree 1:

$$\begin{aligned} T_0(\tau) &= cos(0) = 1 \\ T_1(\tau) &= \tau \end{aligned} \tag{3.6}$$

Chebyshev polynomials of higher degree are calculated using Equation 3.7:

$$\begin{gathered} T_i(\tau) = 2xT_{i-1}(\tau) - T_{i-2}(\tau), \\ i = 2,3,4,5,\ldots \end{gathered} \tag{3.7}$$

In order to ascertain the position of the body, the value of $T_i(\tau)$ is multiplied by the coefficients a_i and subsequently summed (see Equation 3.8). The coefficients are derived from the generic kernels provided by NASA.

$$f(t) = \sum_{i=0}^{n-1} a_i T_i(\tau) \tag{3.8}$$

The Equation 3.8 describes the time-dependent rotation parameters of a celestial body, namely the right ascension (RA) of the North Pole, the declination (DEC) of the North Pole and the prime meridian rotation (W). This enables the celestial body's orientation at any given time to be calculated and translated into a rotation matrix, which is subsequently used for coordinate transformations between body-fixed and inertial systems. Further detailed information can be found in NASA Jet Propulsion Laboratory (n.d.).

This approximation is calculated separately for each vector. Subsequently, the vectors must be added to determine the final position. Figure 3.1 and the Equations 3.9, 3.10, 3.11 and 3.12 illustrate which vectors must be added to obtain the desired result.

The position of the Earth in the BCRS:

$$r_{\text{SBGC}} = r_{\text{SBEMB}} + r_{\text{EMBGC}} \tag{3.9}$$

The position of the station in the BCRS:

$$r_{\text{SBSTA}} = r_{\text{SBEMB}} + r_{\text{EMBGC}} + r_{\text{GCSTA}} \tag{3.10}$$

The position of the Moon in the BCRS:

$$r_{\text{SBSC}} = r_{\text{SBEMB}} + r_{\text{EMBSC}} \tag{3.11}$$

The position of the reflector in the BCRS:

$$r_{\text{SBREF}} = r_{\text{SBEMB}} + r_{\text{EMBSC}} + r_{\text{SCREF}} \tag{3.12}$$

3.2.2 Time Transformation

The LLR analysis is performed in the BCRS, which necessitates the transformation of the observation times into the TDB. The times are initially provided in UTC, and the transformation is conducted in the following order:

$$\text{UTC} \rightarrow \text{TAI} \rightarrow \text{TT} \rightarrow \text{TDB}$$

The transformation from UTC to TT is explained in Chapter 2.4. Using TT instead of TDB as the time argument results in an error of less than 2 ms. Concerning the geocentric position of the Moon, this results in an angular error of less than 1 mas. To achieve greater accuracy, the Python package Skyfield uses Equation 3.13 to transform TT to TDB. The Equation presented in Fairhead and Bretagnon (1990) can be written in a shortened version as

$$\begin{aligned} TDB \approx TT &+ 0.001657 \;\; sin(628.3076T + 6.2401) \\ &+ 0.000022 \;\; sin(575.3385T + 4.2970) \\ &+ 0.000014 \;\; sin(1256.6152T + 6.1969) \\ &+ 0.000005 \;\; sin(606.9777T + 4.0212) \\ &+ 0.000005 \;\; sin(52.9691T + 0.4444) \\ &+ 0.000002 \;\; sin(21.3299T + 5.5431) \\ &+ 0.000010T \;\; sin(628.3076T + 4.2490), \end{aligned} \tag{3.13}$$

where T represents the number of Julian centuries from TT, with the origin set to J2000.0. This can be expressed as T = (JD(TT) - 2 451 545.0)/36 525. The coefficients are expressed in seconds, while the angle arguments are given in radians.

3.2.3 Shapiro Time Delay

In 1964, astrophysicist Irwin I. Shapiro conducted an experiment based on the general theory of relativity to investigate the extent to which light is delayed in the vicinity of massive objects. The light time delay occurs because the speed at which light propagates changes when electromagnetic radiation enters a gravitational field. Consequently, the speed of light differs from the speed it would have in a vacuum. This delay is called the Shapiro time delay (Shapiro, 1964) and is also known as the gravitational time delay.

In LLR analyses, it is essential to consider this delay, as it can lead to inaccuracies in the metre range. The Shapiro time delay must be considered for the Sun and the Earth. The Moon's influence is 1 ps (equivalent to approximately 1 mm for a return trip) and is therefore not considered further (Petit and Luzum, 2010). The calculation of the Shapiro delay is performed using Equation 3.14, derived from Petit and Luzum (2010).

The Shapiro time delay must be considered not only for the laser light pulses in LLR measurements but also for radio waves in VLBI measurements. For detailed information, see Heinkelmann and Schuh (2010).

$$\Delta t = \sum_J \frac{2GM_J}{c^3} ln\left(\frac{r_{J1} + r_{J2} + \rho}{r_{J1} + r_{J2} - \rho}\right) \tag{3.14}$$

The delay is the sum of all relevant bodies J (Sun and Earth) with mass M_J. The distance between the body J and the LLR station labelled „1“ is represented by r_{J1}. r_{J2} describes the distance between the body J and the reflector, labelled „2“. Finally, ρ represents the distance between the station and the reflector. Figure 3.2 illustrates a schematic representation of the Shapiro time delay. „M“ represents the mass, for example, the Sun or the Earth. Unlike the outer red line, where there is no bending, the inner red line shows how the light is diffracted near the mass.

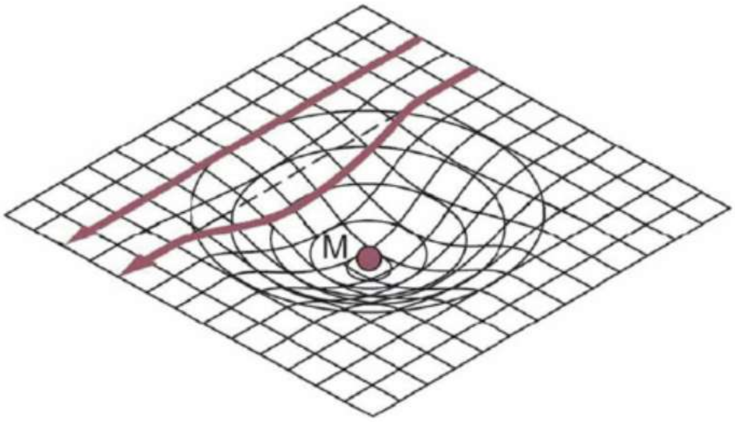

Figure 3.2: Sketch of the Shapiro time delay, from Heinkelmann and Schuh (2010). „M“ visualises the mass. The red lines denote the electromagnetic waves.

Figure 3.3 shows that the Shapiro time delay induced by the Sun in 2019 results in a delay of the Earth-Moon distance between 6.5 and 8 m. The delay depends linearly on the distance between the LLR station and the retroreflector. This is a logical consequence of the laser light pulses being exposed to the Sun's gravitational effects for a longer time. Furthermore, the colour scale indicates that the magnitude is dependent on the Earth's and the Moon's proximity to the Sun. This is quantified by the total distance, which is the sum of the distances from the Earth to the Sun and from the Moon to the Sun. The Shapiro delay is inversely proportional to the distance from the Sun, with a greater total distance resulting in a smaller delay.

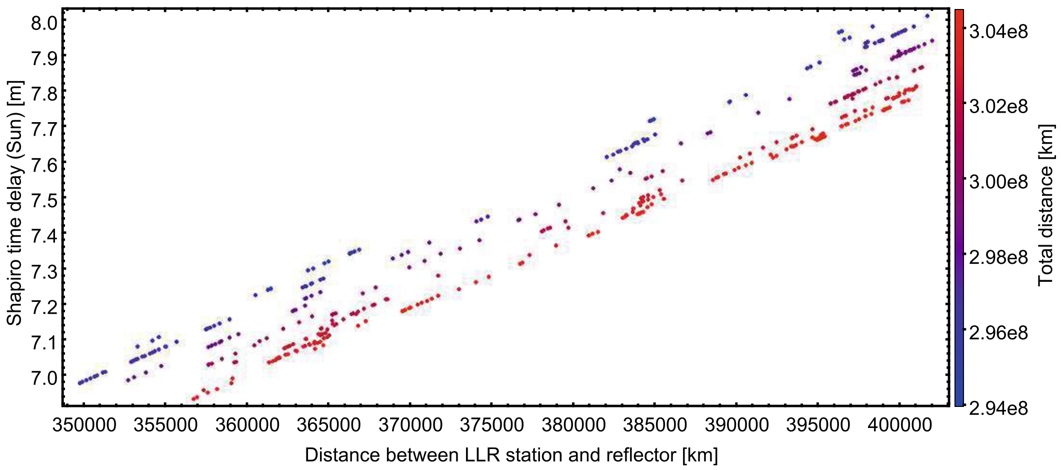

Figure 3.3: The Shapiro time delay, caused by the Sun, is shown as a function of the distance between the Grasse LLR station and the Apollo 15 reflector for 2019. The total distance, represented by a colour bar, is calculated from the sum of the distances between the Earth and the Sun and between the Moon and the Sun.

The Shapiro delay induced by the Earth is considerably less than that induced by the Sun. The resulting values are in the centimetre range. Figure 3.4 depicts the delay as a function of the azimuth. The shape is semicircular, which is a consequence of the fact that at an azimuth of 180°, the station and the reflector are directly opposite each other. Before and after an azimuth of 180°, the signal must traverse the Earth, therefore experiencing a greater influence of the Earth's gravitational field. Moreover, the colour scale illustrates the correlation between the delay and the distance between the station and the reflector. The delay increases proportional to the distance between the station and the reflector.

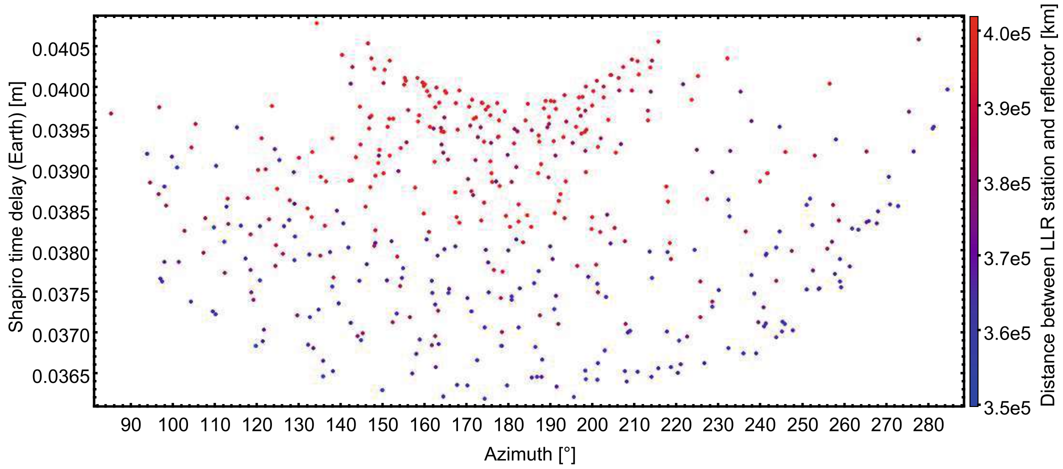

Figure 3.4: The Shapiro time delay, caused by the Earth, is shown as a function of the azimuth between the Grasse LLR station and the Apollo 15 reflector for 2019. The colour bar illustrates the correlation between the delay and the distance between the station and the reflector.

Figure 3.5 illustrates the total Shapiro time delay for 2019. The total Shapiro time delay is the sum of the delays caused by the Sun and the Earth. The monthly variations are attributed to the Moon's orbital motion around the Earth, which results in a changing distance between the two bodies. The rising curve observed towards the end of the year can be attributed to a combination of factors, including the Earth's and Moon's approach towards the Sun during these months.

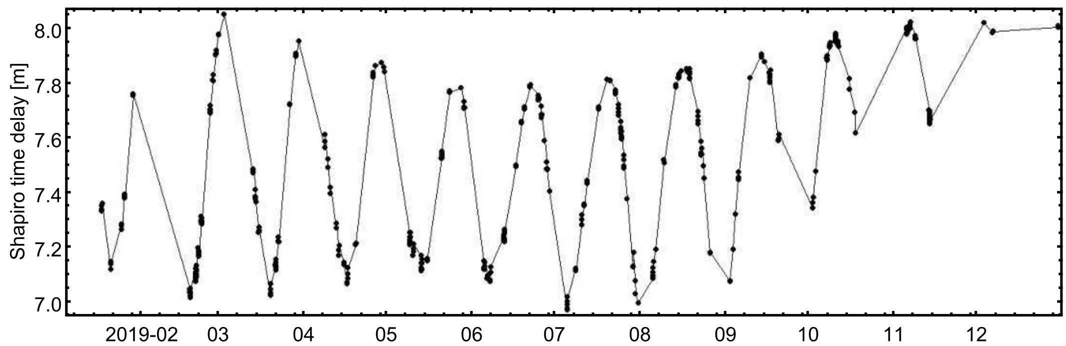

Figure 3.5: Total Shapiro time delay for measurements from the Grasse LLR station to the Apollo 15 reflector for 2019. The total delay is the sum of the delay caused by the Sun and the delay caused by the Earth.

3.2.4 Atmospheric Delay

Geodetic space techniques observe objects in space, whereby the object is either artificially created or represents a natural source. The electromagnetic waves emitted by the source experience a delay in their path through the atmosphere. This delay represents a significant source of error in geodetic space techniques. In order to model these effects, the atmosphere is divided into two layers. The neutral atmosphere extends to an altitude of 100 km, while the ionosphere is located at an altitude of 60 to 2000 km, depending on the location and time. The ionosphere will not be discussed further here, as it is not relevant for processes in the optical range, as is the case with SLR and LLR. In contrast, the neutral atmosphere, which will be referred to as the troposphere in the following, influences electromagnetic waves in the microwave range and on waves in the optical range (Böhm et al., 2013).
However, there is a notable discrepancy in sensitivity between the VLBI and GNSS methods, which operate in the radiowave and microwave range, and the optical methods concerning atmospheric refractivity. While the hydrostatic delay is comparable between the two groups, the non-hydrostatic (wet) delay is 70 times larger for VLBI and GNSS observations than for SLR and LLR observations (Drożdżewski et al., 2019).
This is because optical wavelengths are less sensitive to water vapour. There are typically fewer observations for SLR and LLR than for GNSS and VLBI, so tropospheric parameters are frequently modelled rather than estimated (Boisits et al., 2020).

In this thesis, two models are employed for atmospheric modelling. The first model, as outlined in reference Mendes and Pavlis (2004), calculates the total delay in the zenith direction. The second model, as described in reference Mendes et al. (2002), models the elevation dependence of the travel time delay using a mapping function. The combined models correspond to the standard model for analysing laser ranging data from the ILRS and are consistent with the IERS Conventions 2010.

In order to determine the delay in the zenith direction, the model proposed by Mendes and Pavlis (2004) is employed. This delay is subsequently divided into two distinct components: a hydrostatic and a non-hydrostatic part. The hydrostatic delay, denoted by ΔL_h^z, and the non-hydrostatic delay, represented by ΔL_w^z, are expressed in metres and can be calculated using the Equations 3.15 and 3.16:

$$\Delta L_h^z = 0.002416579 \frac{f_h(\lambda)}{f_s(\Phi, H)} P_s \tag{3.15}$$

$$\Delta L_w^z = 10^{-4} \left(5.316 f_{nh}(\lambda) - 3.759 f_h(\lambda)\right) \frac{e_s}{f_s(\Phi, H)} \tag{3.16}$$

The parameters f_h and f_{nh} represent the hydrostatic and non-hydrostatic components of the dispersion equation, respectively, as a function of the wavelength λ in μm of the laser beam. The expression f_s is a function of the latitude Φ and the geodetic height H of the station. P_s is the surface pressure in hPa and e_s is the surface water pressure in hPa.

In order to obtain the total delay ΔL^z, the sum of the hydrostatic and non-hydrostatic components must be formed, as shown in Equation 3.17.

$$\Delta L^z = \Delta L_h^z + \Delta L_w^z \tag{3.17}$$

To project the delay in zenith direction to a certain elevation angle, the mapping function, called FCULa, is implemented according to the methodology proposed by Mendes et al. (2002) with Equation 3.18. The mapping function is derived from a truncated version of a continued fraction using $1/sin(e)$ (Marini, 1972).

$$m(e) = \frac{1 + \cfrac{a_1}{1 + \cfrac{a_2}{1 + a_3}}}{sin\ e + \cfrac{a_1}{sin\ e + \cfrac{a_2}{sin\ e + a_3}}} \tag{3.18}$$

According to Mendes et al. (2002), the coefficients a_1, a_2, and a_3 are functions of the temperature t_s, the geodetic height H and the latitude Φ of the station (see Equation 3.19). The coefficients a_{ij} are listed in Mendes et al. (2002).

$$a_i = a_{i0} + a_{i1} t_s + a_{i2} cos\Phi + a_{i3} H \tag{3.19}$$

The elevation dependent hydrostatic delay and the wet delay are presented individually in Figure 3.6. The hydrostatic component is responsible for delays in the metre range. In the case of 2019, the values lie between 2 and 8.5 metres. Conversely, the non-hydrostatic component results in delays in the millimetre range. The curve during the summer months can be explained by the increase in humidity at higher temperatures.

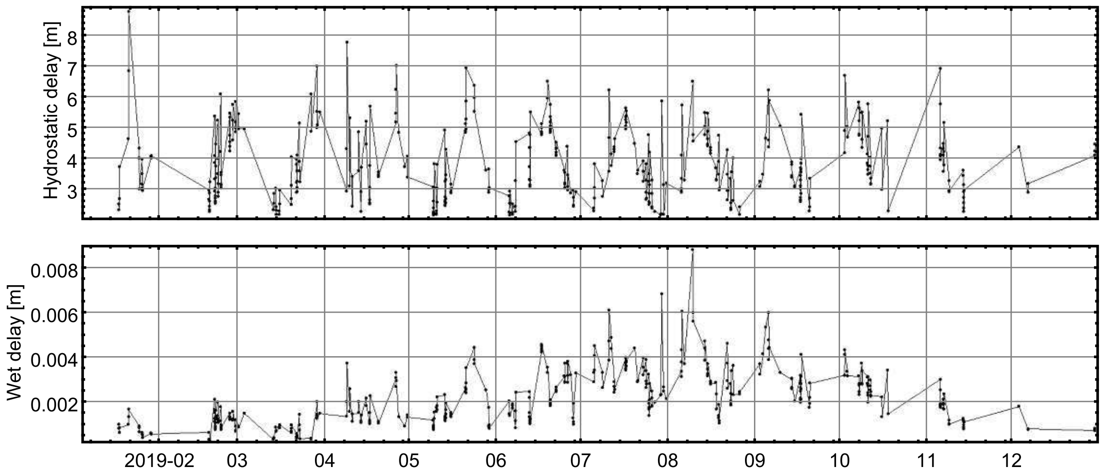

Figure 3.6: The upper plot depicts the hydrostatic delay, while the lower plot illustrates the wet delay for measurements from the Grasse LLR station to the Apollo 15 reflector for 2019.

Figure 3.7 illustrates the total delay for 2019, which is 2 and 9 m for the entire year.

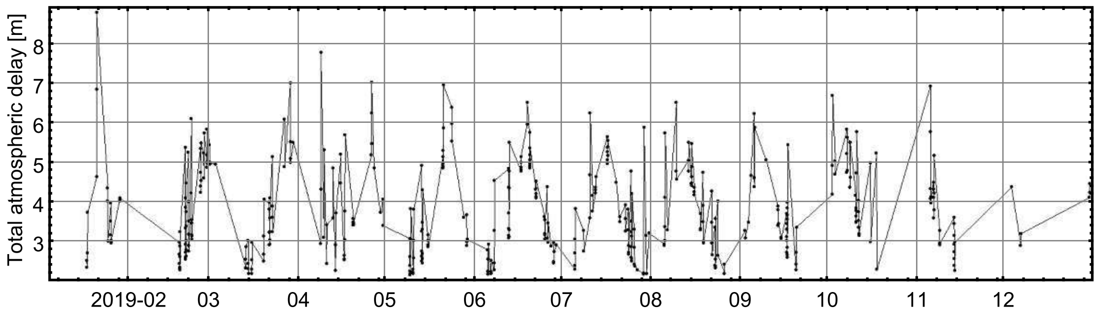

Figure 3.7: Total atmospheric delay, defined as the sum of the hydrostatic and wet delays, for measurements from the Grasse LLR station to the Apollo 15 reflector for 2019.

Figure 3.8, demonstrates the influence of the elevation on the total atmospheric delay in 2019. The decrease in elevation leads to an increase in the delay.

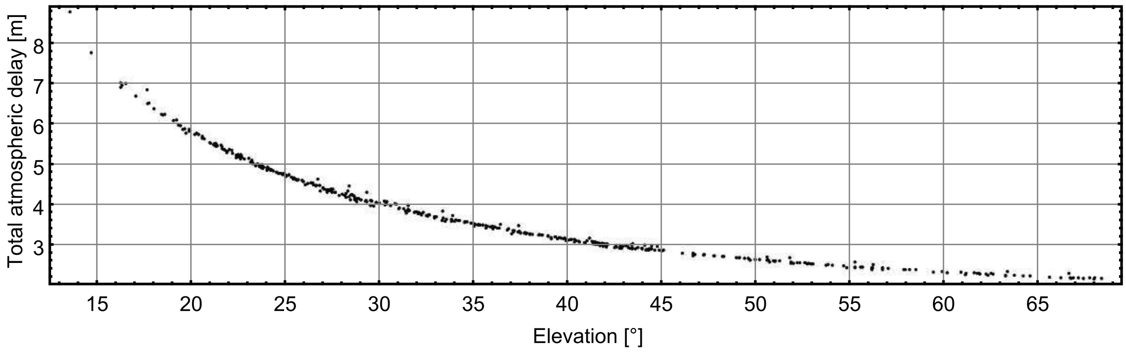

Figure 3.8: Total atmospheric delay as a function of the elevation for measurements from the Grasse LLR station to the Apollo 15 reflector for 2019.

3.2.5 Residuals

This section presents the calculated residuals. The residuals are the differences between the measured and calculated values (o-c) and can be seen in Figure 3.9 for 2011 to 2021. The term „raw" refers to the difference produced when the atmospheric correction and the Shapiro time delay caused by the Sun and the Earth are not considered. The discrepancies range from 9 to 18 m. When the atmosphere is taken into account, the residuals reduce to 6 to 9 m. Subsequently, the Shapiro time delay of the Earth is incorporated, which impacts the differences in the centimetre range. Finally, the Shapiro time delay of the Sun is considered, resulting in residuals within the range of -1 to 1 m.

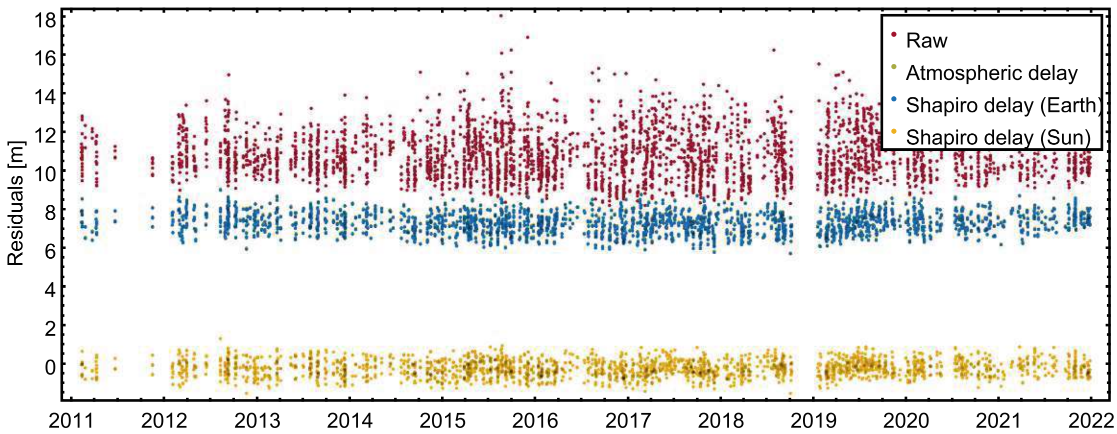

Figure 3.9: Residuals (o-c) of the measurements from the Grasse LLR station to the Apollo 15 reflector from 2011 to 2021. The corrections for the delays are added to the „raw residuals" in descending order.

Figure 3.10 illustrates the residuals for 2019. It can be observed that a periodic trend is present in the raw residuals, which is a consequence of the continuous alteration in the distance between the Earth and the Moon and the associated impact of the gravitational fields of the Sun and the Earth. However, this periodic trend is no longer evident after correcting for the Shapiro time delay.

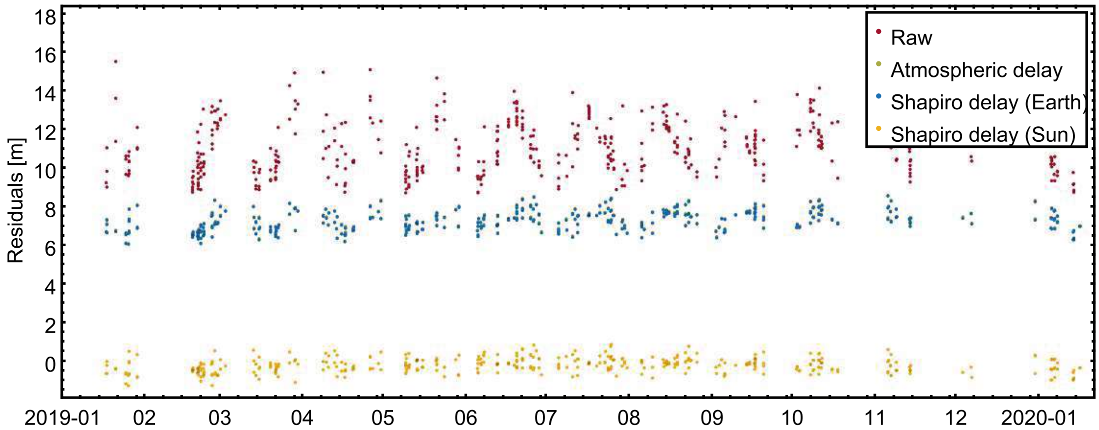

Figure 3.10: Residuals (o-c) of the measurements from the Grasse LLR station to the Apollo 15 reflector for 2019. The corrections for the delays are added to the „raw residuals“ in descending order.

LLR observations have been made since 1969. Over time, the technology has continuously improved and as a result, the accuracy of the measurements has increased (Hofmann et al., 2015).
The Figures 3.11 and 3.12 provide statistical summaries of the calculated residuals. In Figure 3.11, boxplots of the residuals from 2011 to 2021 are presented. The number of normal points is given by „n“. The median of the residuals is between 0 and -5 dm in all years. 50% of the residuals range from 5 to 7 dm, while the remaining 50% are up to 10 or -15 dm. A few residuals are more significant and are indicated as outliers (circles).
Finally, Figure 3.12 illustrates the number of observations and the Root Mean Square (RMS) for each year from 1984 to 2021, based on data from POLAC. In 2006, 2007 and 2008, no observations were made from the Grasse LLR station to the Apollo 15 reflector. Before 2002, the RMS value exceeded 1 m for multiple years. However, from 2002 onwards (except for 2006, 2007 and 2008), the RMS value consistently fell below 1 m. Between 2015 and 2021, the RMS value was less than half a metre.

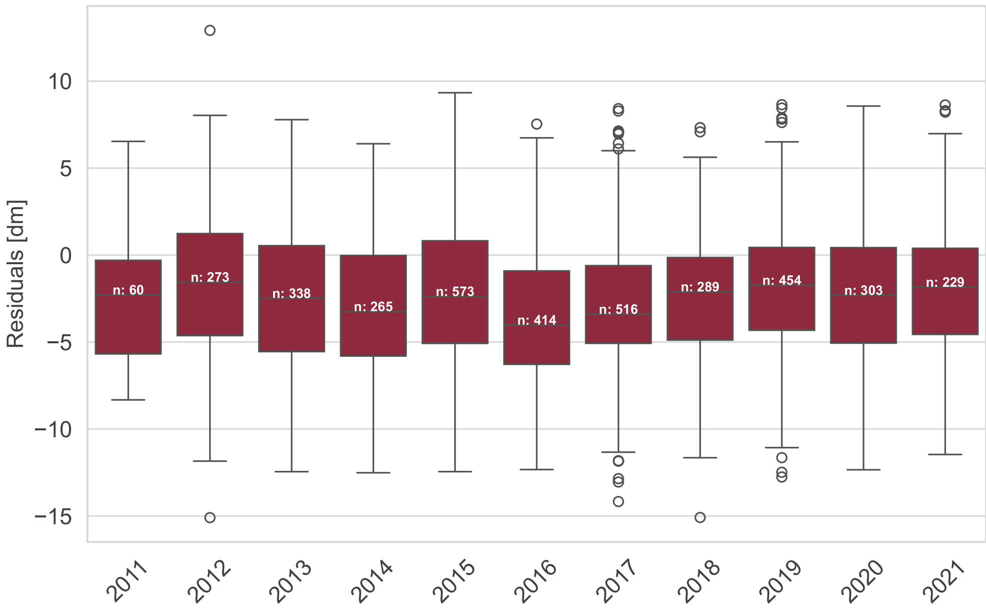

Figure 3.11: Boxplots of the residuals for measurements from the Grasse LLR station to the Apollo 15 reflector from 2011 to 2021.

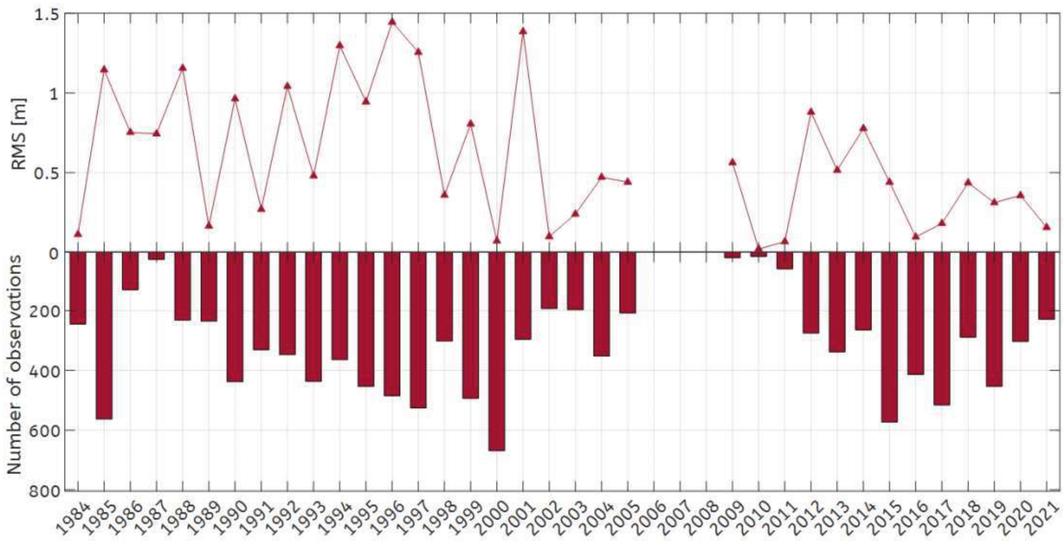

Figure 3.12: Number of observations and RMS values per year for measurements from the Grasse LLR station to the Apollo 15 reflector from 1984 to 2021.

4 Visibility analysis for a VLBI Transmitter on the Moon

To optimise the efficiency of future VLBI observations of the Moon, it is essential to determine precisely when the transmitter will be visible and the duration of the visibility. Furthermore, it is crucial to ascertain the number of stations that can see the transmitter simultaneously. For this purpose, the scheduling software VieSched++ has been modified. In this thesis, the primary criteria for determining the visibility of the VLBI transmitter are the elevation and the number of stations from which the visibility is given.

4.1 Software VieSched++

As outlined in Chapter 2.1.2, scheduling is a crucial aspect of conducting VLBI observations. The software VieSched++ was developed for this purpose at the Department of Geodesy and Geoinformation at the Technische Universität Wien (TU Wien). The software is written in C++ and comprises two distinct components: a graphical user interface (GUI) and the scheduler (Schartner and Böhm, 2019).

VieSched++ is capable of scheduling typical VLBI observations of quasars. Wolf (2021) extended the software also to enable the incorporation of satellite observations. For this thesis, VieSched++ was adapted so that it is now possible to determine the exact position of the VLBI transmitter on the Moon. This is the first step towards expanding the software to include a Moon observation module. This will then enable future Moon observations to be scheduled together with satellite and quasar observations. The position of the VLBI transmitter on the Moon was determined in VieSched++ using the SPICE Toolkit from NASA. The outcomes align with the Python computations based on the Skyfield package, as presented in Chapter 3.

4.2 VLBI Station Network

The visibility study is conducted utilising eight VLBI stations. The locations of the VLBI stations are illustrated in Figure 4.1. The selected stations are part of the observation network of the IVS-R1 or IVS-R4 sessions. The IVS-R1 and IVS-R4 sessions are each 24 hours long and take place on Mondays (IVS-R1) and Thursdays (IVS-R4), respectively. The stations were selected to ensure optimal global distribution. Five of the total number of stations are situated in the Northern Hemisphere, while the remaining four are located in the Southern Hemisphere. The following stations are included in the network, with the IVS code and the country in which the VLBI station is located provided for each:

- KOKEE (Kk, USA)
- WESTFORD (Wf, USA)
- FORTLEZA (Ft, Brazil)
- NYALES20 (Ny, Norway)
- WETTZ13N (Wn, Germany)
- HARTRAO (Hh, South Africa)
- BADARY (Bd, Russia)
- HOBART12 (Hb, Australia)

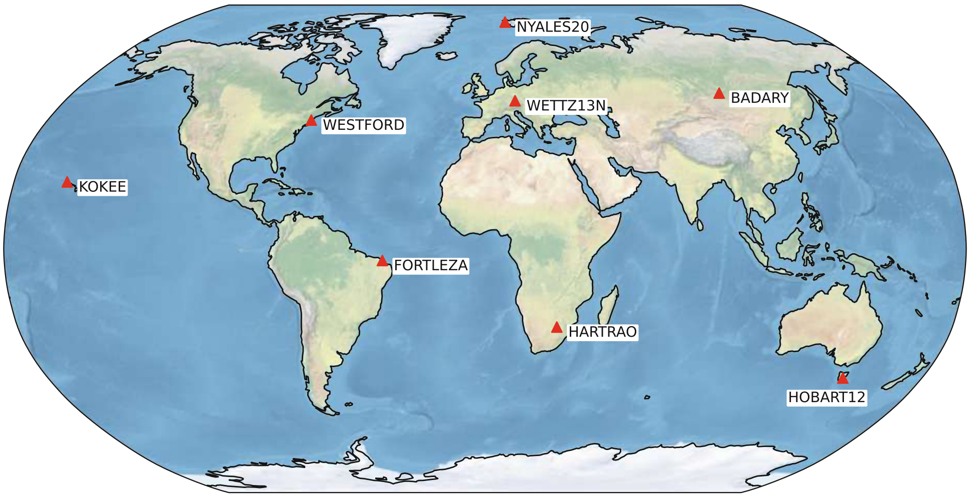

Figure 4.1: Positions of the VLBI stations for the visibility study. The selected VLBI stations are regularly part of IVS-R1 or IVS-R4 sessions.

4.3 Position of the VLBI Transmitter on the Moon

As previously outlined in Section 3.1.2, no official position of a potential VLBI transmitter on the Moon has been made public so far. However, for this study, as with the LLR analysis presented in Chapter 3, the position of the Apollo 15 LLR reflector is assumed for the VLBI transmitter. The position of the Apollo 15 reflector on the Moon can be seen in Figure 2.4.

4.4 Evaluation of Visibility

The Earth-Moon system is characterised by a high degree of dynamism, with the Moon's orbit continuously changing. To see how significant the fluctuation is within a year, Figure 4.2 illustrates the sublunar point every 24 hours for 2023. Each month is visualised in a different colour. The sublunar point is the point on Earth where the Moon's centre is at its zenith.

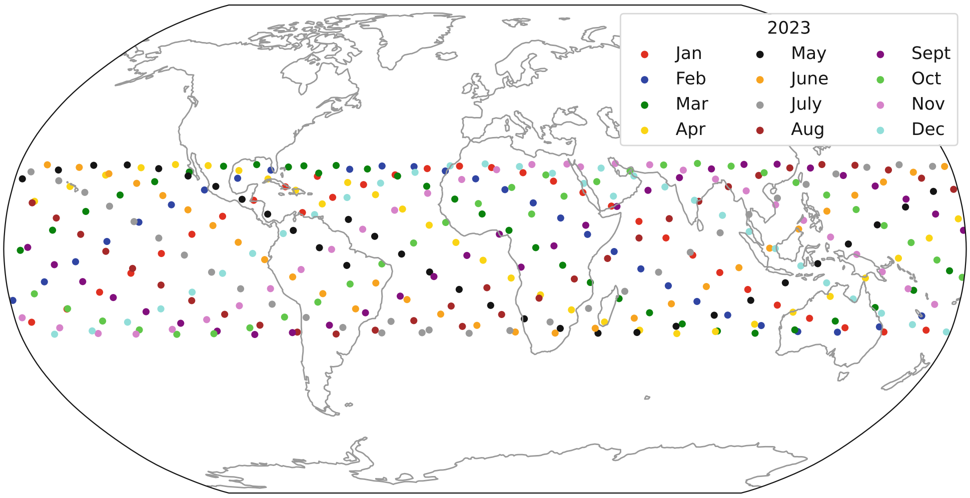

Figure 4.2: Sublunar point on Earth for 2023, with a resolution of 24 hours. The points show where the Moon is at its zenith on Earth.

In general, the visibility between a VLBI station and a VLBI transmitter is given if the VLBI transmitter is above the horizon. In other words, the elevation must be $> 0°$. However, due to the hardware limitations of the antenna axis, a cut-off angle of 5° has been determined in this thesis. The Figures 4.3 and 4.5 provide a comprehensive overview of the number of hours per day during which the VLBI transmitter was visible from all stations in 2021, 2022 and 2023. Several disparate patterns can be discerned. The visibility patterns observed for the three VLBI stations WETTZ13N, WESTFORD and BADARY in the Northern Hemisphere (see Figure 4.3) and the VLBI station HOBART12 in the Southern Hemisphere (see Figure 4.5) are notably variable. In several consecutive days, the visibility period is limited to approximately 6 to 8 hours, followed by days when visibility increases to 12 to 16 hours. In contrast, the telescopes KOKEE, FORTLEZA and HARTRAO exhibit a more uniform pattern. The visibility is constant throughout the year, between 10 and 14 hours. An extreme case is the station NYALES20 (see figure 4.4). Due to its northern location, this station reaches a visibility of 0 to 24 hours per day and is displayed with its own colour scale. The movement and rotation of the Earth and the Moon change the pattern between 2021, 2022 and 2023 for all stations.

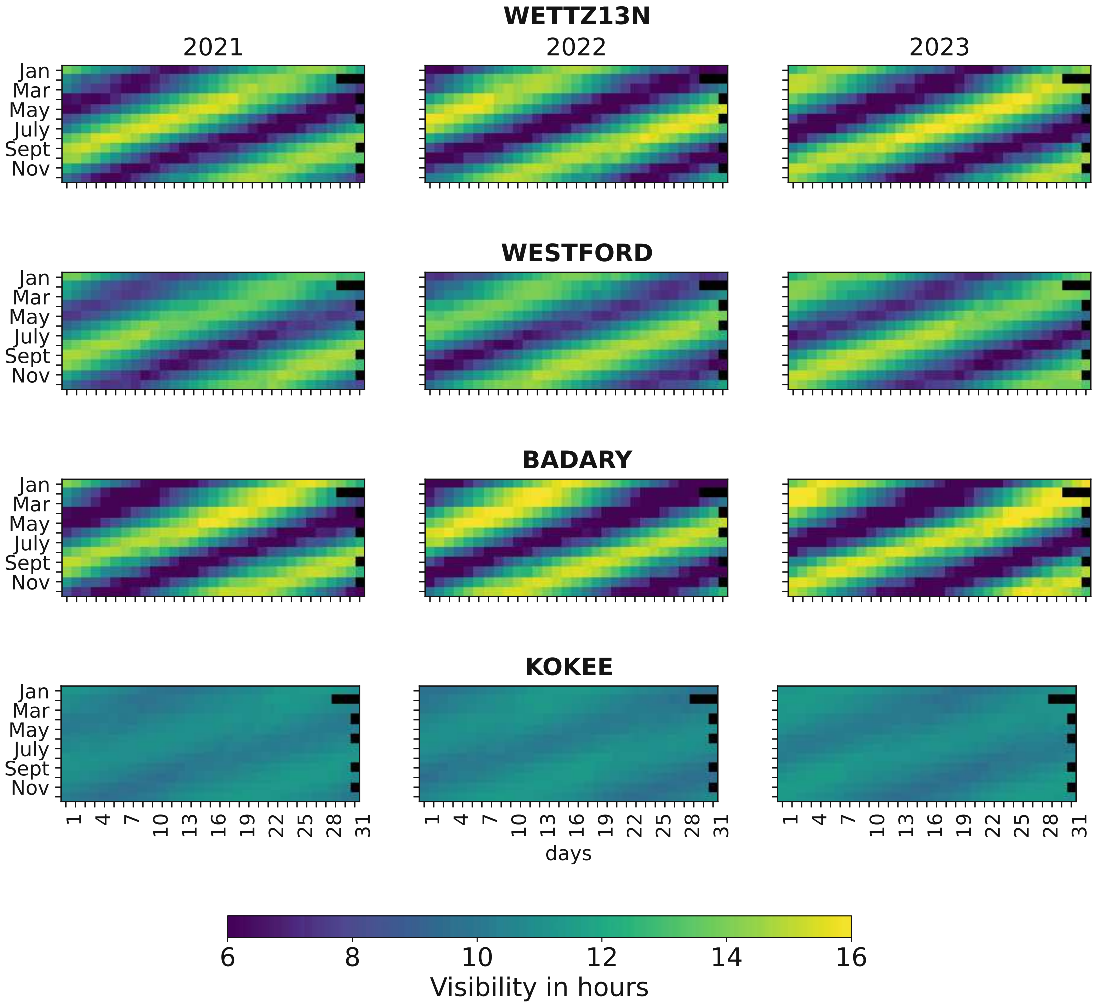

Figure 4.3: Visibility of the VLBI transmitter from VLBI stations in the Northern Hemisphere for 2021, 2022 and 2023. The VLBI transmitter is considered visible if it has an elevation of $\geq 5°$ from the station. The black fields result from not every month having 31 days.

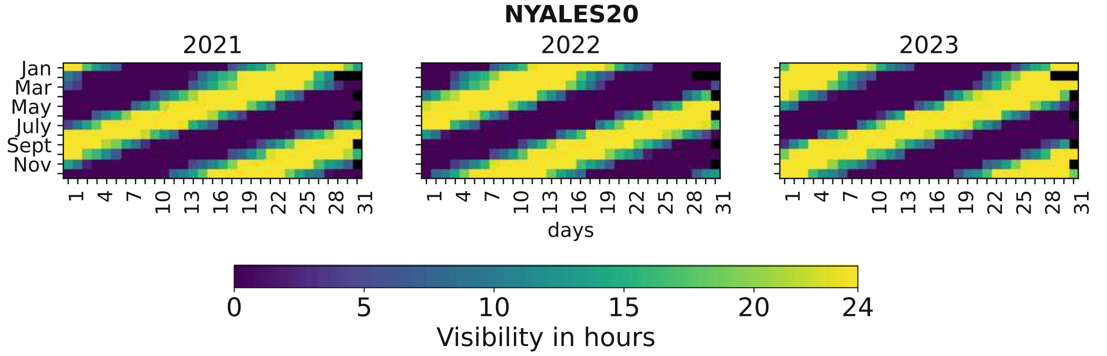

Figure 4.4: Visibility of the VLBI transmitter from the VLBI station NYALES20 for 2021, 2022 and 2023. The VLBI transmitter is considered visible if it has an elevation of $\geq 5°$ from the station. The black fields result from not every month having 31 days.

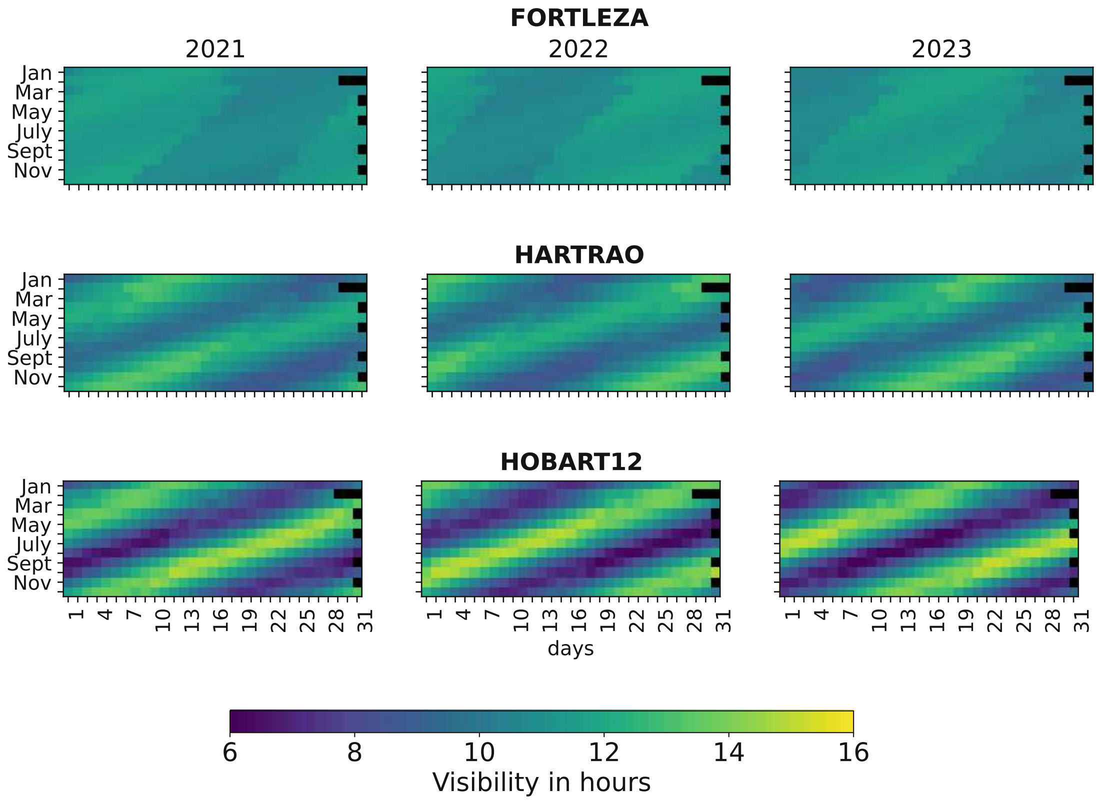

Figure 4.5: Visibility of the VLBI transmitter from VLBI stations in the Southern Hemisphere for 2021, 2022 and 2023. The VLBI transmitter is considered visible if it has an elevation of $\geq 5°$ from the station. The black fields result from not every month having 31 days.

In order to facilitate a more comprehensive analysis of visibility, four hypothetical sessions have been created for the dates 6 January 2023, 6 April 2023, 6 July 2023 and 6 October 2023. These sessions start at 18:30:00 UTC and conclude the subsequent day at the same time. The elevations of the individual stations relative to the VLBI transmitter on the Moon are illustrated in Figures 4.6, 4.7, 4.8 and 4.9. Blue shades indicate the VLBI stations in the Northern Hemisphere, while various shades of red indicate the VLBI stations in the Southern Hemisphere.
A comparison of the elevation plots with the Figures 4.3, 4.4 and 4.5 reveals a logical correlation. Stations with a line of sight to the VLBI transmitter for only a few hours on the days achieve only a low elevation. It can be observed that stations for which the transmitter is visible for a longer period achieve a higher elevation. Furthermore, the plots illustrate the significance of ensuring a global comprehensive and balanced distribution of stations, encompassing both latitudinal and longitudinal considerations.

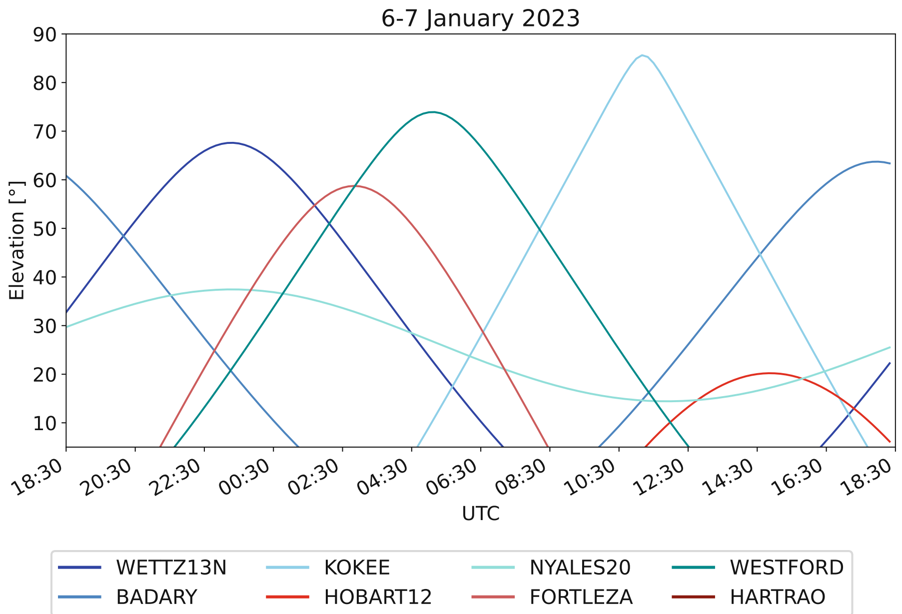

Figure 4.6: Elevation from each VLBI station to the VLBI transmitter for the 24-hour session on 6 January 2023, starting at 18:30:00 UTC. The stations situated in the Northern Hemisphere are indicated by different shades of blue, while those located in the Southern Hemisphere are represented by different shades of red.

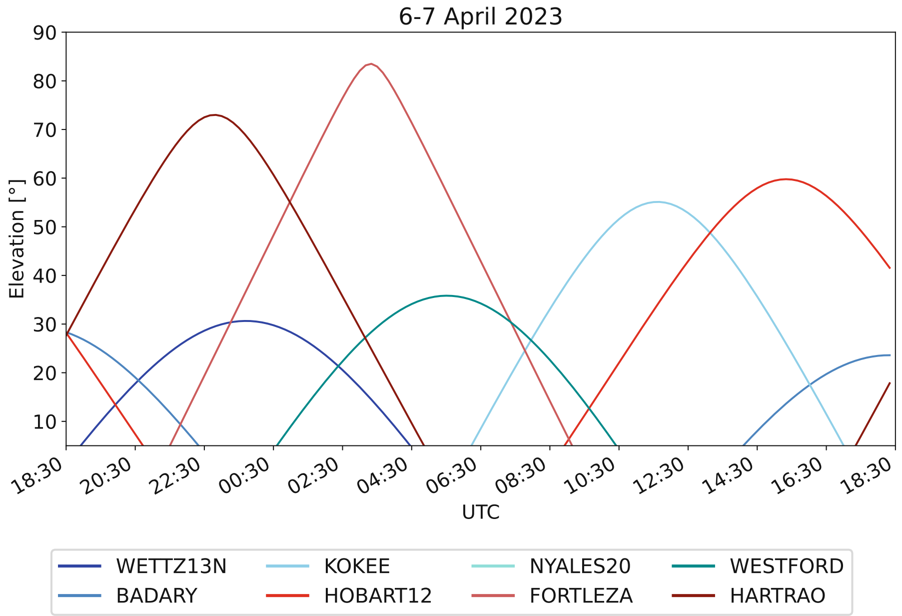

Figure 4.7: Elevation from each VLBI station to the VLBI transmitter for the 24-hour session on 6 April 2023, starting at 18:30:00 UTC. The stations situated in the Northern Hemisphere are indicated by different shades of blue, while those located in the Southern Hemisphere are represented by different shades of red.

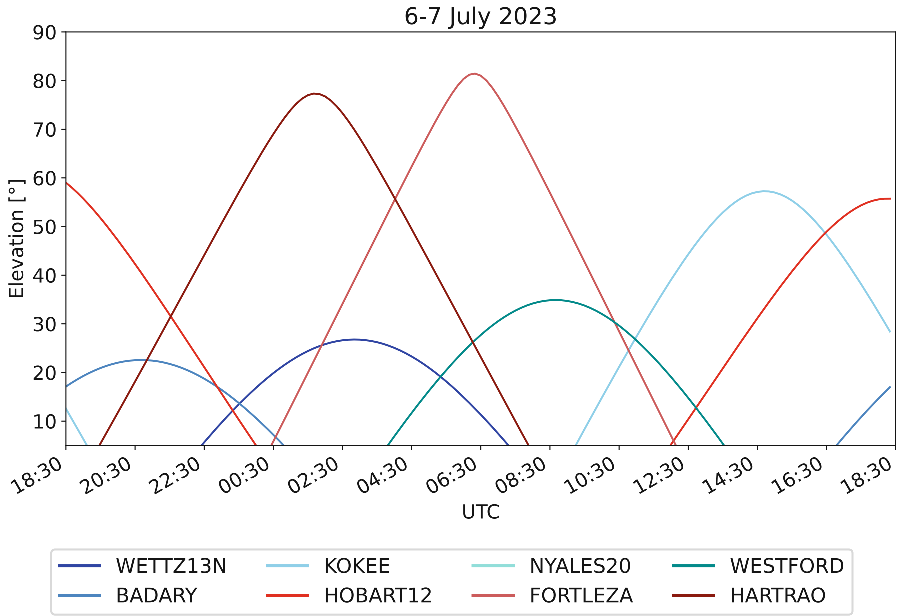

Figure 4.8: Elevation from each VLBI station to the VLBI transmitter for the 24-hour session on 6 July 2023, starting at 18:30:00 UTC. The stations situated in the Northern Hemisphere are indicated by different shades of blue, while those located in the Southern Hemisphere are represented by different shades of red.

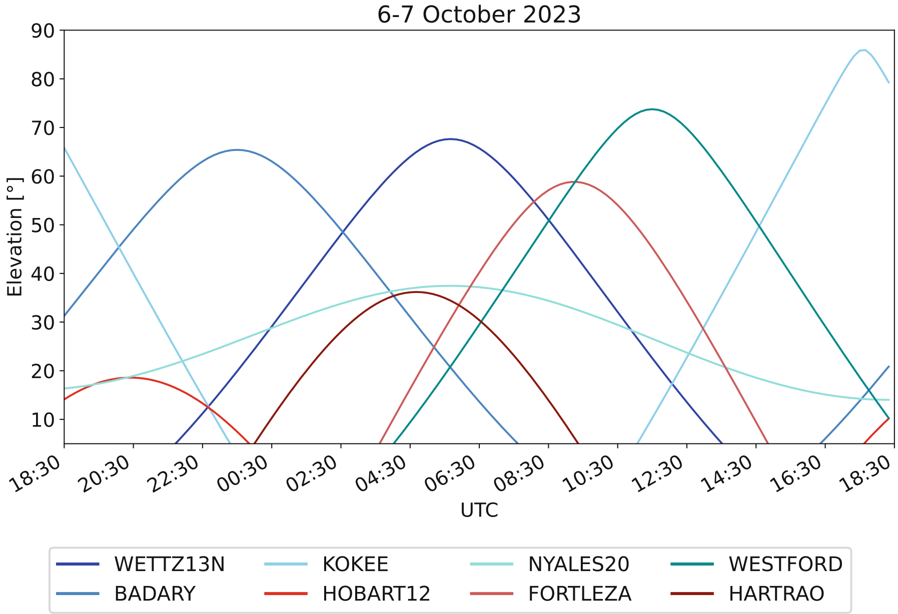

Figure 4.9: Elevation from each VLBI station to the VLBI transmitter for the 24-hour session on 6 October 2023, starting at 18:30:00 UTC. The stations situated in the Northern Hemisphere are indicated by different shades of blue, while those located in the Southern Hemisphere are represented by different shades of red.

As outlined in Chapter 2.1.1, at least two radio telescopes must observe the same radio source simultaneously. VieSched++ was therefore employed to ascertain the precise temporal windows during which the stations can observe the VLBI transmitter. This considers the elevation angle to be ≥5° and other parameters.

For some VLBI antennas, a so-called „horizon mask“ indicates the minimum elevation required for each azimuth. The elevation can exceed the previously used 5° cut-off angle, for instance, due to hardware limitations or the presence of nearby objects that cause shadowing (Schartner, 2019).

The Figures 4.10, 4.11, 4.12 and 4.13 show the time windows of visibility of the individual VLBI stations for the four sessions. The colour blue indicates the stations located in the Northern Hemisphere, while the colour red is used to indicate stations located in the Southern Hemisphere. The northern stations can observe the VLBI transmitter more often during the sessions in January and October. During the sessions in April and July, the southern stations enjoy longer periods of visibility. Moreover, it can be observed that during the sessions in January and October, the VLBI transmitter is continuously visible from the NYALES20 station for 24 hours. In contrast, during the sessions in April and July, the VLBI transmitter is never visible from the NYALES20 station. The smaller gaps, for example, at the KOKEE station in the April and July sessions, are due to the horizon mask mentioned above. The VLBI transmitter would be above 5° elevation here, but the minimum elevation for azimuths between 107° and 153° for the KOKEE station is 25° (taken from the horizon mask catalogue mask.cat).

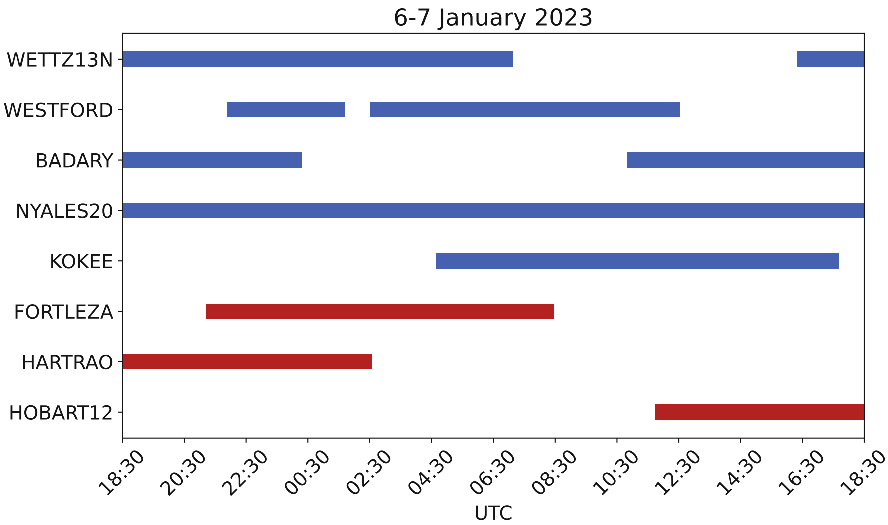

Figure 4.10: Time windows for the 24-hour session on 6 January 2023, starting at 18:30:00 UTC, when the visibility is given between the VLBI station and the VLBI transmitter. The stations situated in the Northern Hemisphere are indicated by the colour blue, while those located in the Southern Hemisphere are represented by the colour red.

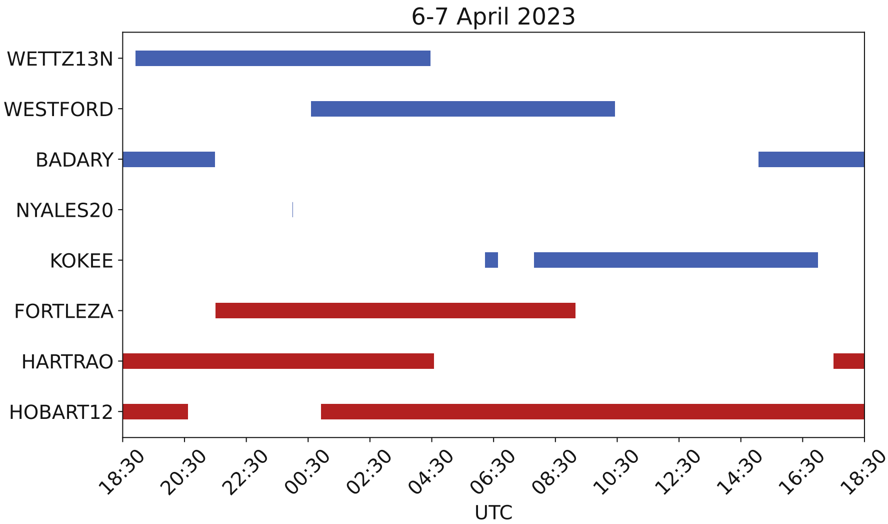

Figure 4.11: Time windows for the 24-hour session on 6 April 2023, starting at 18:30:00 UTC, when the visibility is given between the VLBI station and the VLBI transmitter. The stations situated in the Northern Hemisphere are indicated by the colour blue, while those located in the Southern Hemisphere are represented by the colour red.

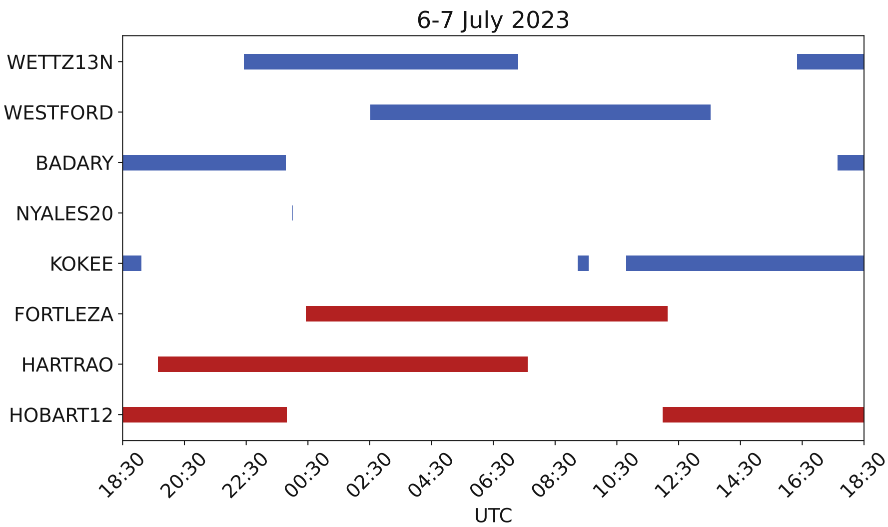

Figure 4.12: Time windows for the 24-hour session on 6 July 2023, starting at 18:30:00 UTC, when the visibility is given between the VLBI station and the VLBI transmitter. The stations situated in the Northern Hemisphere are indicated by the colour blue, while those located in the Southern Hemisphere are represented by the colour red.

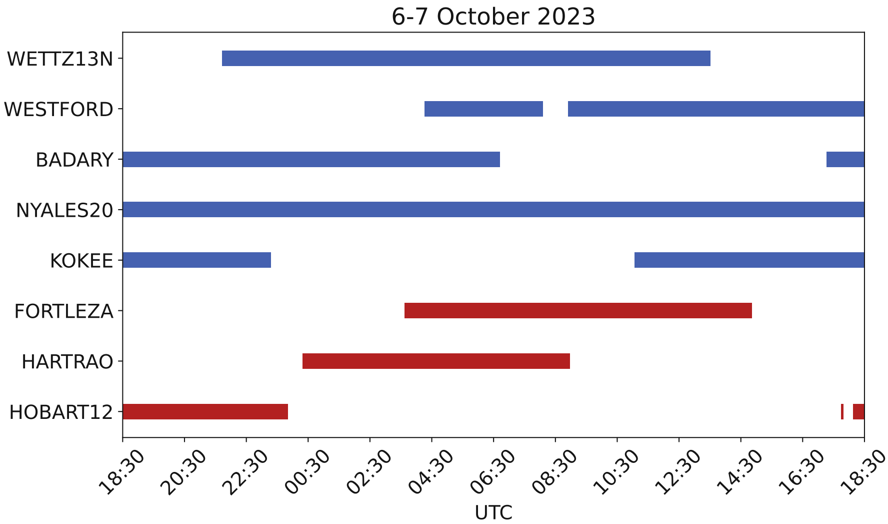

Figure 4.13: Time windows for the 24-hour session on 6 October 2023, starting at 18:30:00 UTC, when the visibility is given between the VLBI station and the VLBI transmitter. The stations situated in the Northern Hemisphere are indicated by the colour blue, while those located in the Southern Hemisphere are represented by the colour red.

As mentioned, at least two radio telescopes must simultaneously observe a source. For this purpose, Figure 4.14 illustrates the number of VLBI stations with a simultaneous line of sight to the VLBI transmitter. Concerning the session in January, the minimum number of stations with visibility is two, while the maximum number of stations is six. In the April session, the minimum number of stations is two, and the maximum is five stations. In the July session, up to four stations may have a line of sight at any given time. At the beginning of the session, a single station is granted a line of sight. Furthermore, the October session again exhibits a higher mean number of stations with a line of sight to the VLBI transmitter. The maximum number of stations is six, while the minimum is one. Compared with the Figures 4.10, 4.11, 4.12 and 4.13, a greater number of stations than just one or two should have a line of sight at the beginning of the sessions. However, a line of sight is available for some stations only a few seconds after the session begins.

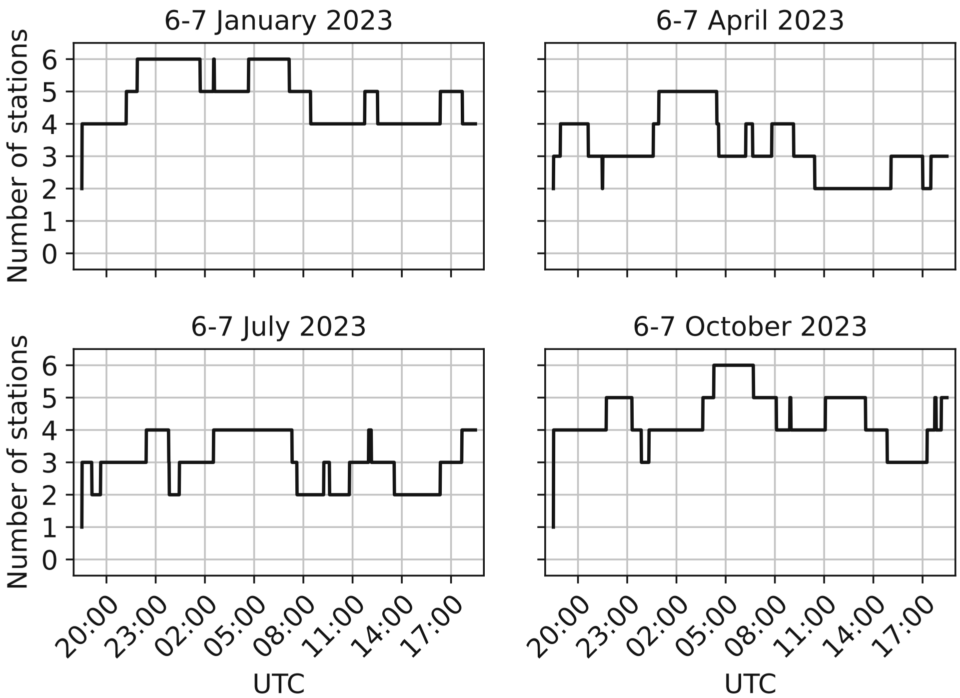

Figure 4.14: Number of VLBI stations with simultaneous line of sight to the VLBI transmitter for the 24-hour sessions on 6 January 2023, 6 April 2023, 6 July 2023 and 6 October 2023, each starting at 18:30:00 UTC.

5 Conclusions and Prospects for Future Studies

The Moon has become a subject of great scientific interest, which is why several future missions have been planned. In recent years, the concept of a VLBI transmitter on the Moon has emerged. This thesis, therefore, deals with the models that form the foundation for future analysis of VLBI observations to the Moon in VieVS. The models are validated by analysing LLR measurements from the Grasse LLR station to the Apollo 15 reflector. This process is also an essential first step towards analysing LLR observations in VieVS and combining VLBI and LLR measurements.

For the LLR analysis, it is first necessary to transform the position of the LLR station on Earth and the reflector position on the Moon into the BCRS. Furthermore, the start time, reflection time and reception time of the laser light pulse must be transformed into TDB. The reflection time on the Moon and the reception time on Earth are calculated iteratively. The laser light pulses experience a temporal delay on their journey to the Moon and back. It is essential to model these delays to achieve optimal accuracy in the LLR analysis. This thesis considers the effects of atmospheric delay and Shapiro time delay. The atmospheric correction is in the range of 2 to 9 m. The Shapiro time delay caused by the Sun leads to delays in the range of 6 to 8 m, whereas the Shapiro time delay caused by the Earth is a few centimetres. Considering these effects, the resulting residuals range from -1 to +1 m from 2002 (no measurements from the Grasse LLR station to the Apollo 15 reflector are available for 2006, 2007 and 2008).

The second part of the thesis is a visibility analysis. For this purpose, the scheduling software VieSched++ was modified. This investigation aims to determine the frequency and duration of visibility of the fictitious VLBI transmitter from eight selected VLBI stations for 2021, 2022 and 2023. The visibility is given when the VLBI transmitter has an elevation of at least $\geq 5^{\circ}$ above the horizon. In order to ensure a representative sample, a VLBI network with a good global distribution of stations was selected. The results demonstrate that stations such as WETTZ13N, WESTFORD, BADARY and HOBART12 exhibit a considerable degree of variability in visibility duration. On some days, the visibility period is as low as 6 to 8 hours, while on other days, it can reach up to 16 hours. The KOKEE and FORTLEZA stations show a relatively consistent pattern. The VLBI transmitter is consistently visible in these locations for approximately 10 to 12 hours daily. The NYALES20 station is a notable exception due to its highly northerly location. The visibility duration of the VLBI transmitter varies for this VLBI station from 0 to 24 hours. The study shows that the visibility period of the VLBI transmitter strongly depends on the Moon's position and the location of the VLBI station on Earth. This implies that a comprehensive global distribution of VLBI stations is crucial. While a balanced north-south distribution is fundamental, an even east-west distribution is equally important.

Given the inherent complexity of VLBI observations to the Moon, mainly due to the Earth-Moon system's dynamic nature, further investigation is necessary. For instance, Sert (2023) examines the optimal location on the Moon for installing the VLBI transmitter and the VLBI network geometry that yields the highest accuracy in measurements. Subsequently, VieSched++ and VieVS could be expanded to incorporate a module for the Moon, enabling the scheduling, simulation, and analysis of combined observations of quasars, satellites, and the Moon.

References

Acton, C., Bachman, N., Semenov, B., & Wright, E. (2018). A look towards the future in the handling of space science mission geometry [Enabling Open and Interoperable Access to Planetary Science and Heliophysics Databases and Tools]. *Planetary and Space Science*, *150*, 9–12. https://doi.org/https://doi.org/10.1016/j.pss.2017.02.013

Acton, C. H. (1996). Ancillary data services of NASA's Navigation and Ancillary Information Facility [Planetary data system]. *Planetary and Space Science*, *44*(1), 65–70. https://doi.org/https://doi.org/10.1016/0032-0633(95)00107-7

Altamimi, Z., Rebischung, P., Collilieux, X., Métivier, L., & Chanard, K. (2022). ITRF2020 [Data set]. IERS ITRS Center Hosted by IGN and IPGP [https://doi.org/10.18715/IPGP.2023.LDVIOBNL, Accessed: (July 2023)].

Archinal, B., Acton, C., A'Hearn, M., Conrad, A., Consolmagno, G., Duxbury, T., Hestroffer, D., Hilton, J., Kirk, R., Klioner, S., McCarthy, D., Meech, K., Oberst, J., Ping, J., Seidelmann, P., Tholen, D., Thomas, P., & Williams, I. (2018). Report of the iau working group on cartographic coordinates and rotational elements: 2015. *Celestial Mechanics and Dynamical Astronomy*, *130*. https://doi.org/10.1007/s10569-017-9805-5

Archinal, B. A., IAU WG on Cart. Coord., & Rot. Elements. (2024). Updating the Cartographic Lunar Reference Frame. *55th Lunar and Planetary Science Conference*, *3040*, Article 1696, 1696.

Artz, T. (2011). *Determination of Sub-daily Earth Rotation Parameters from VLBI Observations* [Doctoral dissertation, Rheinische Friedrich-Wilhelms-Universität Bonn]. https://hdl.handle.net/20.500.11811/4757

Barache, C., Bouquillon, S., Bourgoin, A., Carlucci, T., & Francou, G. (2021). Observatoire de Paris (SYRTE): Paris Observatory Lunar Analysis Centre (POLAC) [Accessed: (November 2023)].

Biskupek, L. (2015). *Bestimmung der Erdorientierung mit Lunar Laser Ranging* [Doctoral dissertation, Gottfried Wilhelm Leibniz Universität Hannover] [Dissertation]. Verlag der Bayerischen Akademie der Wissenschaften. https://doi.org/10.15488/4721

Böhm, J., Salstein, D. A., Alizadeh, M., & Wijaya, D. D. (2013). Geodetic and Atmospheric Background. In J. Böhm & H. Schuh (Eds.), *Atmospheric effects in space geodesy* (pp. 1–34). Springer Verlag.

Böhm, J., & Wolf, H. (2024). Opportunities with VLBI Transmitters on Satellites. Springer Berlin Heidelberg. https://doi.org/10.1007/1345_2024_240

Boisits, J., Landskron, D., & Böhm, J. (2020). VMF3o: the Vienna Mapping Functions for optical frequencies. *Journal of Geodesy*, *94*. https://doi.org/10.1007/s00190-020-01385-5

Condie, K. C. (2011). 9 - Great Events in Earth History. In K. C. Condie (Ed.), *Earth as an evolving planetary system (second edition)* (Second Edition, pp. 357–435). Academic Press. https://doi.org/https://doi.org/10.1016/B978-0-12-385227-4.00002-X

Courde, C., Torre, J. M., Samain, E., Martinot-Lagarde, G., Aimar, M., Albanese, D., Exertier, P., Fienga, A., Mariey, H., Metris, G., Viot, H., & Viswanathan, V. (2017). Lunar laser ranging in infrared at the Grasse laser station. *A&A*, *602*, A90. https://doi.org/10.1051/0004-6361/201628590

Crease, R. P. (2019). How high the Moon. *Physics World*, *32*(7), 26. https://doi.org/10.1088/2058-7058/32/7/27

Creech, S., Guidi, J., & Elburn, D. (2022). Artemis: An Overview of NASA's Activities to Return Humans to the Moon. *2022 IEEE Aerospace Conference (AERO)*, 1–7. https://doi.org/10.1109/AERO53065.2022.9843277

Delva, P., Blazquez, A., Bloßfeld, M., Böhm, J., Bonnefond, P., Boy, J.-P., Bruinsma, S., Bury, G., Chatzinikos, M., Couhert, A., Courde, C., Dach, R., Dehant, V., Dell'Agnello, S., Elgered, G., Enderle, W., Exertier, P., Glaser, S., & Zajdel, R. (2022). GENESIS: Co-location of Geodetic Techniques in Space. https://doi.org/10.48550/arXiv.2209.15298

Drożdżewski, M., Sośnica, K., Zus, F., & Balidakis, K. (2019). Troposphere delay modeling with horizontal gradients for satellite laser ranging. *Journal of Geodesy*, *93*(10), 1853–1866. https://doi.org/10.1007/s00190-019-01287-1

Eppler, D. B., & Budden, N. A. (2018). Lighting Constraints to Lunar Surface Operations. In LPI Editorial Board (Ed.), *Survive and operate through the lunar night workshop* (p. 7008, Vol. 2106).

Fairhead, L., & Bretagnon, P. (1990). An analytical formula for the time transformation TB-TT. *Astronomy and Astrophysics*, *229*, 240–247.

Gorkavyi, N., Krotkov, N., & Marshak, A. (2023). Earth observations from the moon's surface: Dependence on lunar libration. *Atmospheric Measurement Techniques*, *16*(6), 1527–1537. https://doi.org/10.5194/amt-16-1527-2023

Heinkelmann, R., & Schuh, H. (2010). Very Long Baseline Interferometry (VLBI): Accuracy limits and relativistic tests. https://doi.org/10.1017/S1743921309990524

Hellmers, H., Modiri, S., Bachmann, S., Thaller, D., Bloßfeld, M., Seitz, M., & Gipson, J. (2023). Combined IVS Contribution to the ITRF2020. In J. T. Freymueller & L. Sánchez (Eds.), *Geodesy for a sustainable earth* (pp. 3–13). Springer International Publishing.

Hofmann, F., Müller, J., & Biskupek, L. (2015). Lunar Laser Ranging: Das Erde-Mond-System und Tests der Einstein'schen Gravitationstheorie. *140*(6), 337–345. https://doi.org/10.12902/zfv-0087-2015

Kellermann, K. I., Bouton, E. N., & Brandt, S. S. (2020). A New Window on the Universe. In *Open skies: The national radio astronomy observatory and its impact on us radio astronomy* (pp. 1–34). Springer International Publishing. https://doi.org/10.1007/978-3-030-32345-5_1

Kłopotek, G., Hobiger, T., & Haas, R. (2017). Geodetic VLBI with an artificial radio source on the Moon: a simulation study. *Journal of Geodesy*, *92*, 457–469. https://doi.org/10.1007/s00190-017-1072-4

Kłopotek, G., Hobiger, T., Haas, R., Jaron, F., La Porta, L., Nothnagel, A., Zhang, Z., Han, S., Neidhardt, A., & Plötz, C. (2019). Position determination of the Chang'e 3 lander with geodetic VLBI. *Earth Planets and Space*, *71*. https://doi.org/10.1186/s40623-019-1001-2

Liu, S., Yan, J., He, Q., Cao, J., Ye, M., & Barriot, J.-P. (2020). Precise positioning of Chang'e 3 lander based on Helmert-VCE-aided weighting method using phase delay data from Chinese VLBI Network. *Advances in Space Research*, *66*. https://doi.org/10.1016/j.asr.2020.05.034

Liu, S., Rogers, J., & Jacintho, J. (1980). *Improved Chebyshev series ephemeris generation capability of GTDS*.

Marini, J. W. (1972). Correction of Satellite Tracking Data for an Arbitrary Tropospheric Profile [Cited by: 184]. *Radio Science*, *7*(2), 223–231. https://doi.org/10.1029/RS007i002p00223

McCall, G. (2005). EARTH STRUCTURE AND ORIGINS. In R. C. Selley, L. R. M. Cocks, & I. R. Plimer (Eds.), *Encyclopedia of geology* (pp. 421–429). Elsevier. https://doi.org/https://doi.org/10.1016/B0-12-369396-9/00464-0

McCarthy, D. (1998). The Julian and Modified Julian Dates. *Journal for the History of Astronomy*, *29*, 327. https://doi.org/10.1177/002182869802900402

Mendes, V. B., & Pavlis, E. C. (2004). High-accuracy zenith delay prediction at optical wavelengths. *Geophysical Research Letters*, *31*(14). https://doi.org/https://doi.org/10.1029/2004GL020308

Mendes, V. B., Prates, G., Pavlis, E. C., Pavlis, D. E., & Langley, R. B. (2002). Improved mapping functions for atmospheric refraction correction in SLR. *Geophysical Research Letters*, *29*(10), 53-1-53–4. https://doi.org/https://doi.org/10.1029/2001GL014394

Met Office. (2010). *Cartopy: a cartographic python library with a matplotlib interface*. Exeter, Devon. https://scitools.org.uk/cartopy

Müller, J., Murphy, T., Schreiber, K., Shelus, P., Torre, J.-M., Williams, J., Boggs, D., Bouquillon, S., Bourgoin, A., & Hofmann, F. (2019). Lunar Laser Ranging: a tool for general relativity, lunar geophysics and Earth science. *Journal of Geodesy*, *93*. https://doi.org/10.1007/s00190-019-01296-0

Munghemezulu, C., Combrinck, L., Mayer, D., & Botai, J. (2014). Comparison of Site Velocities Derived from Collocated GPS, VLBI and SLR Techniques at The Hartebeesthoek Radio Astronomy Observatory (Comparison of Site Velocities). *Journal of Geodetic Science*, *4*, 1–7. https://doi.org/10.2478/jogs-2014-0002

Murphy, T. W. (2013a). Lunar laser ranging: the millimeter challenge. *Reports on Progress in Physics*, *76*(7), 076901. https://doi.org/10.1088/0034-4885/76/7/076901

Murphy, T. W. (2013b). Lunar laser ranging: the millimeter challenge. *Reports on Progress in Physics*, *76*(7), 076901. https://doi.org/10.1088/0034-4885/76/7/076901

Murphy, T. W., Adelberger, E. G., Battat, J. B. R., Carey, L. N., Hoyle, C. D., LeBlanc, P., Michelsen, E. L., Nordtvedt, K., Orin, A. E., Strasburg, J. D., Stubbs, C. W., Swanson, H. E., & Williams, E. (2008). The Apache Point Observatory Lunar Laser-ranging Operation: Instrument Description and First Detections. *Publications of the Astronomical Society of the Pacific*, *120*(863), 20–37. Retrieved April 8, 2024, from http://www.jstor.org/stable/10.1086/526428

NASA Jet Propulsion Laboratory. (n.d.). PCK File Required Reading [Accessed: 2024-09-09].

Nelson, R., McCarthy, D., Malys, S., Levine, J., Guinot, B., Fliegel, H., Beard, R., & Bartholomew, T. (2003). The Leap Second: Its History and Possible Future. *Metrologia*, *38*, 509. https://doi.org/10.1088/0026-1394/38/6/6

Park, R. S., Folkner, W. M., Williams, J. G., & Boggs, D. H. (2021). The JPL Planetary and Lunar Ephemerides DE440 and DE441. *The Astronomical Journal*, *161*(3), 105. https://doi.org/10.3847/1538-3881/abd414

Petit, G., Arias, F., & Panfilo, G. (2015). International atomic time: Status and future challenges [The measurement of time / La mesure du temps]. *Comptes Rendus*

Physique, *16*(5), 480–488. https://doi.org/https://doi.org/10.1016/j.crhy.2015.03.002

Petit, G., & Luzum, B. (2010). IERS Conventions (2010). *IERS Technical Note*, *36*, 1.

Rhodes, B. (2019). Skyfield: High precision research-grade positions for planets and Earth satellites generator.

Saleh, A.-R. (2018). Synodic Month. *Iraqi Journal of Science*.

Schartner, M., & Böhm, J. (2019). VieSched++: A New VLBI Scheduling Software for Geodesy and Astrometry. *Publications of the Astronomical Society of the Pacific*, *131*(1002), 084501. https://doi.org/10.1088/1538-3873/ab1820

Schartner, M. (2019). *Optimizing geodetic VLBI schedules with VieSched++* [Doctoral dissertation, Technische Universität Wien]. https://doi.org/10.34726/hss.2019.49542

Schuh, H., & Behrend, D. (2012). VLBI: A fascinating technique for geodesy and astrometry. *Journal of Geodynamics*, *61*, 68–80. https://doi.org/https://doi.org/10.1016/j.jog.2012.07.007

Schuh, H., & Böhm, J. (2013). Very Long Baseline Interferometry for Geodesy and Astrometry. In G. Xu (Ed.), *Sciences of geodesy - ii: Innovations and future developments* (pp. 339–376). Springer Berlin Heidelberg. https://doi.org/10.1007/978-3-642-28000-9_7

Sert, H. (2023). LNP-VLBI Transmitter on the Moon. Report for the Scientific Work Package. Following Statement of Work document N°: LNP-VLBI-AS-SOW-0002 Issue 01.00. *ROB/AWS (Belgium)*.

Shapiro, I. I. (1964). Fourth test of general relativity. *Phys. Rev. Lett.*, *13*, 789–791. https://doi.org/10.1103/PhysRevLett.13.789

Soffel, M., Klioner, S. A., Petit, G., Wolf, P., Kopeikin, S. M., Bretagnon, P., Brumberg, V. A., Capitaine, N., Damour, T., Fukushima, T., Guinot, B., Huang, T.-Y., Lindegren, L., Ma, C., Nordtvedt, K., Ries, J. C., Seidelmann, P. K., Vokrouhlický, D., Will, C. M., & Xu, C. (2003). The IAU 2000 Resolutions for Astrometry, Celestial Mechanics, and Metrology in the Relativistic Framework: Explanatory Supplement. *The Astronomical Journal*, *126*(6), 2687. https://doi.org/10.1086/378162

Soffel, M., & Langhans, R. (2013). *Space-Time Reference Systems*. https://doi.org/10.1007/978-3-642-30226-8

Taylor, M. B. (2005). TOPCAT & STIL: Starlink Table/VOTable Processing Software. In P. Shopbell, M. Britton, & R. Ebert (Eds.), *Astronomical data analysis software and systems xiv* (p. 29, Vol. 347).

Vokrouhlický, D. (1997). A Note on the Solar Radiation Perturbations of Lunar Motion. *Icarus*, *126*(2), 293–300. https://doi.org/https://doi.org/10.1006/icar.1996.5652

Wolf, H. (2021). *Satellite Scheduling with VieSched++* [Master's thesis, Technische Universität Wien]. https://doi.org/10.34726/hss.2021.87526

Wolf, H., & Böhm, J. (2023). Optimal distribution of VLBI transmitters in the Galileo space segment for frame ties. *Earth, planets, and space : EPS*, *75*, 173. https://doi.org/10.1186/s40623-023-01926-0

Wolf, H., Böhm, J., Schartner, M., Hugentobler, U., Soja, B., & Nothnagel, A. (2023). Dilution of Precision (DOP) Factors for Evaluating Observations to Galileo Satellites with VLBI [Publisher Copyright: © 2022, The Author(s).; Scientific Assembly of the International Association of Geodesy, IAG 2021 ; Conference date: 28-06-2021 Through 02-07-2021]. In J. Freymueller & L. Sánchez (Eds.), *Geodesy for a sustainable earth - proceedings of the 2021 scientific assembly of the international association of geodesy* (pp. 305–312). Springer Science; Business Media Deutschland GmbH. https://doi.org/10.1007/1345_2022_165

Zhao, X., Zheng, W.-M., Tong, L., & Ma, M.-L. (2022). Dual-target Signal Simulation of Very Long baseline Interferometry for Chang'E-5. *Publications of the Astronomical Society of the Pacific*, *134*(1038), 084502. https://doi.org/10.1088/1538-3873/ac8579